3.09 Nanostructures and Surface-Enhanced Raman Spectroscopy

K M Kosuda, J M Bingham, K L Wustholz, and R P Van Duyne, Northwestern University, Evanston, IL, USA

3.09.1   Introduction

A major focus in the field of nanoscience is the optical properties of metallic nanostructures. Excitation of the localized surface plasmon resonance (LSPR) of metallic surfaces having nanoscale features results in local electromagnetic (EM) field enhancement. This field enhancement has dramatic effects on molecules adsorbed to the surface of plasmonic nanostructures. More than 30 years ago, it was recognized that the Raman scattering intensity of pyridine on electrochemically roughened Ag was enhanced by $\sim 10^6$ [1, 2]. This remarkable discovery led to the emergence of surface-enhanced Raman spectroscopy (SERS), a technique that proved to be a powerful tool for fundamental studies of surface adsorbates. However, the analytical utility of SERS was limited early on, owing to problems with irreproducibility and uncertainty regarding the origin of large enhancements. In the years following the discovery of SERS, intensive research focused on achieving a mechanistic understanding of SERS, which is now understood to be dominated by an EM field enhancement mechanism. Advances in nanofabrication methods that produce substrates with controlled and well-defined plasmonic properties, along with improvements in laser sources, detection schemes, and theoretical modeling provide the basis for our current understanding of SERS. In addition, the discovery of single-molecule SERS (SMSERS) in 1997 [3, 4] has generated heightened interest in both the fundamentals of the technique as well as its application to chemical analysis. SERS has developed into a sensitive analytical tool for the detection of molecules adsorbed on nanostructures, and surface modification techniques have also allowed for improved analyte selectivity. To date, SERS has been used to probe chemical problems in areas as diverse as chemistry, physics, materials science, surface science, catalysis, electrochemistry, and life sciences.

This chapter is aimed at providing a sound background for understanding the relationship between nanostructures and SERS. We first introduce the physical basis of the LSPR, with particular attention to the dielectric function of plasmonic materials as it relates to nanoparticle extinction. Experimental and computational methods of evaluating nanoparticle extinction are briefly presented. We then review various methods for the fabrication of nanostructures that support LSPRs, including chemical syntheses, laser ablation, and lithographic techniques. Factors that affect nanoparticle extinction, including nanoparticle size and shape, refractive index of the nanoparticle environment, distance dependence of the LSPR, as well as coupling among nanoparticles, are summarized with experimental examples. We then discuss a new approach to the functionalization and stabilization of nanostructures using atomic layer deposition (ALD). In particular, ultrathin Al_2O_3 films are shown to significantly protect nanoparticles from thermal annealing, laser damage, and solvent-induced structural changes.

We next focus on the fundamentals and applications of SERS. The origin of SERS enhancement is reviewed with particular emphasis on the EM mechanism. A brief discussion of enhancement factor (EF) calculation is also presented. We then describe two important consequences of the EM mechanism, the distance dependence (probed via ALD experiments) and excitation-wavelength dependence of SERS. The results of surface-enhanced Raman excitation spectroscopy experiments for resonant and nonresonant molecules reveal the important relationship between LSPR and SERS enhancement. Next, we highlight advances in the field of SMSERS. The isotopologue approach to proving SMSERS detection is presented, followed by studies aimed at elucidating the structure of SMSERS hot spots as well as evaluating the relative contributions of EM and resonance Raman enhancement to single-molecule sensitivity. We then discuss progress in the application of SERS to chemical problems, focusing specifically on *in vivo* glucose sensing, art conservation, and detection of chemical and biological warfare agents.

Finally, we turn our attention to the future of SERS. The investigation of new plasmonic materials as well as novel nanostructures promises to broaden the scope of SERS. In particular, understanding the fundamental relationships between nanostructures

and their resulting optical properties is an important goal, both from a fundamental and practical standpoint. Correlated investigations of nanoparticle structure – LSPR and SERS – will ultimately enable the rational design of high-enhancing SERS substrates. We also discuss an important variation of SERS, tip-enhanced Raman spectroscopy (TERS), which combines the sensitivity and rich chemical information of SERS with the excellent spatial resolution of scanning probe microscopy. Given the advantages of complete surface generality, spatial resolution of ∼10 nm, and near single-molecule sensitivity [5, 6], it is anticipated that TERS will be a powerful tool for probing chemical problems in many areas. The progress of research highlighted in this chapter points to a promising future in which SERS will have a significant impact on the field of nanoscience and technology.

3.09.2   Localized Surface Plasmon Resonance Spectroscopy

The LSPR is the phenomenon responsible for the brilliant colors exhibited by Ag and Au nanoparticles under illumination. These brightly colored particles have been of interest to artisans since antiquity and are responsible for the color in the Roman Lycurgus Cup [7, 8] as well as antique stained-glass windows. Scientific interest in metallic particles dates back to Michael Faraday in the nineteenth century when he examined size and color changes of Au particles [9]. To understand SERS and its capabilities, it is important to review the underlying mechanism for surface enhancement, namely the LSPR. This section provides a theoretical and experimental background of LSPR. We hope to highlight the significance of LSPR

in relation to SERS and provide a sound foundation for the following SERS section in this chapter.

Surface plasmon resonance (SPR) is found in materials that have a negative real and small positive imaginary dielectric constant. In most instances, SPR occurs in metals like Ag and Au. When EM radiation is incident on these metals, it induces a collective oscillation of surface conduction electrons – a resonance. Significant attention has been focused on surface plasmons and their use for biological and chemical sensing, as well as surface-enhanced spectroscopies. In SPR spectroscopy, thin metal films (∼50 nm thick) support surface-propagating plasmons, also referred to as surface plasmon polaritons (SPPs). The SPPs propagate ten to hundreds of microns in the x- and y-directions along the metal–dielectric interface and decay evanescently in the z-direction on the order of 200 nm. A variation of SPR is LSPR, which has been of particular interest since the advent of nanofabrication techniques. When surface plasmons are confined to a nanostructure much smaller than the wavelength of light, they are localized around the nanostructure with a specific frequency known as the LSPR. **Figure 1** depicts the difference between SPR and LSPR [10].

Both SPR and LSPR are sensitive to the surrounding dielectric environment and, consequently, both SPR and LSPR are used for sensing experiments. A more thorough theoretical description of these sensitivities is presented in Section 3.09.2.1.3. Although at present SPR spectroscopy leads LSPR in commercial development, LSPR has comparable attributes [10, 11] and is superior to SPR in many cases [10, 12, 13]. For example, SPR measurements are more sensitive to bulk changes in refractive index due to the significantly shorter EM field decay length of LSPR, but LSPR surpasses SPR on the absolute
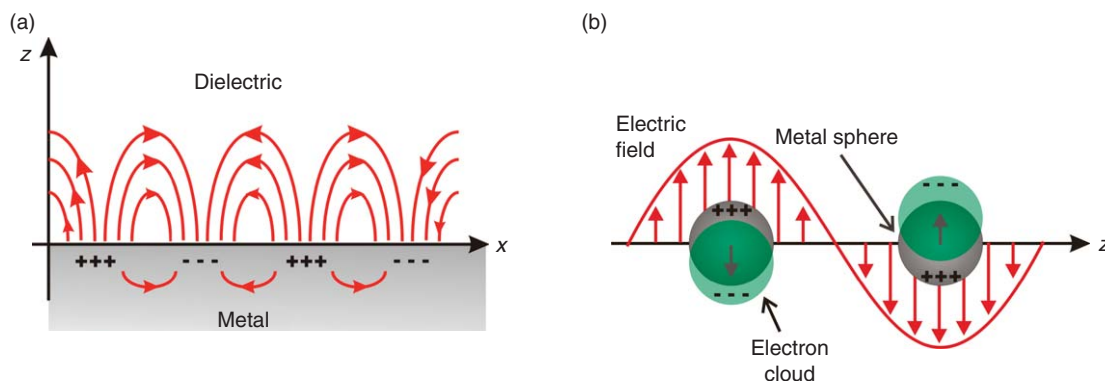
Figure 1   Schematic diagrams for (a) SPR and (b) LSPR.

number of molecules detected if metal surface areas are taken into consideration [10]. The advancement of nanofabrication techniques has enabled numerous new LSPR applications and is discussed in more detail in Section 3.09.2.2. Moreover, LSPR is a main contributor to surface enhancement and is described more thoroughly in the following sections to provide a detailed understanding of SERS.

3.09.2.1 Theory

Brightly colored nanoparticles have been of interest to both the artistic and scientific communities. Therefore, it was quite significant when Gustav Mie presented a solution to Maxwell's equations that described the extinction spectra (where extinction = scattering + absorption) of spherical particles of arbitrary size, providing a classical explanation for the brilliant colors of metallic nanoparticles [14]. Mie's solutions have proved to be even more valuable over time and are a sound starting point for analyses of nonspherical particles [15], as Richard Gans extended Mie's solutions to Au spheroidal particles [16] in 1912 and to Ag spheroidal particles [17] in 1915. It is important to note that Mie's solutions to Maxwell's equations are often referred to as 'Mie theory', although the solutions do not address an independent physical phenomenon. Additionally, Mie theory is sometimes referred to as Lorenz–Mie theory or Lorenz–Mie–Debye theory, but for consistency with existing literature, the term Mie theory is used hereafter.

3.09.2.1.1 Solution to Maxwell's equations: Mie theory

When metallic nanoparticles are irradiated by light, the oscillating electric field causes a collective oscillation of the conduction electrons in the metal. The Coulombic attraction between the negatively charged electrons and positively charged nuclei (and repulsion among electrons) causes a restoring force to arise when the electron cloud is displaced relative to the nuclei, resulting in an oscillation of the electron cloud [15, 18, 19]. The coherent oscillation is called the dipole plasmon resonance or the LSPR and the plasmon resonant frequency is related to the metal dielectric constant that is measured as a function of wavelength for bulk metal [15]. To understand the relationship between the plasmon frequency and metal dielectric constant, the electric field surrounding the particle is considered. Here, the

conditions used in Mie theory to solve Maxwell's equations for the EM field outside the particle are described, although a complete annotated derivation is described elsewhere [10]. The equation to describe the EM field outside a particle can be derived using the following limits. Briefly, the particle under consideration is spherical, with radius a, and is irradiated by z-polarized light with a corresponding wavelength, λ. In this case, a is much smaller than the wavelength of light (i.e., $a/\lambda < 0.1$), such that the electric field is approximated as constant (or static) around the nanoparticle (**Figure 1**) [10, 15]. In this 'quasi-static' approximation, the interaction is dictated by electrostatics instead of electrodynamics, but the dielectric constant of the metallic particle changes with wavelength [15]. In this approximation, the electric and magnetic components are decoupled, allowing for independent analysis of each, but the magnetic component contributes negligibly compared to the electric component [20]. Therefore, only the electric component of the EM field needs to be considered and not the magnetic component, and consequently, all future references to the EM field refer to the electric field component [10]. The electric field of the incident EM wave propagating in the z-direction is denoted by E_0 such that $E_0 = E_0\hat{\mathbf{z}}$, where $\hat{\mathbf{z}}$ is a unit vector. Solving LaPlace's equation, a fundamental equation of electrostatics, and applying boundary conditions for inside and outside the sphere, the following equation is obtained for the electric field outside a spherical particle [10, 15]:

$$E_{\text{out}}(x, y, x) = E_0\hat{\mathbf{z}} - \alpha E_0 \left[\frac{\hat{\mathbf{z}}}{r^3} - \frac{3z}{r^5}(x\hat{\mathbf{x}} + y\hat{\mathbf{y}} + z\hat{\mathbf{z}}) \right] \quad (1)$$

In **equation 1**, r is the distance from the center of the particle, α is the polarizabiltiy, and $\hat{\mathbf{x}}$, $\hat{\mathbf{y}}$, and $\hat{\mathbf{z}}$ are unit vectors [15]. The first term in **equation 1** represents the incident field and the second term corresponds to the induced dipole field. The induced dipole moment is $\mu_{\text{ind}} = \alpha E_0$, where $\alpha = g_d a^3$ and

$$g_d = \frac{\varepsilon_{\text{in}} - \varepsilon_{\text{out}}}{\varepsilon_{\text{in}} + 2\varepsilon_{\text{out}}} \quad (2)$$

In **equation 2**, g_d describes the polarizability of the metal particle's dielectric function (ε_{in}) and the external dielectric constant (ε_{out}) [15]. Substituting the induced dipole moment equation into **equation 1**, the solution to Maxwell's equations for the electric field outside a particle using the quasi-static approximation is [10, 15]:

$$E_{out}(x, y, x) = E_0\hat{\mathbf{z}} - \left[\frac{\varepsilon_{in} - \varepsilon_{out}}{\varepsilon_{in} + 2\varepsilon_{out}}\right] \times \alpha^3 E_0 \left[\frac{\hat{\mathbf{z}}}{r^3} - \frac{3z}{r^5}(x\hat{\mathbf{x}} + y\hat{\mathbf{y}} + z\hat{\mathbf{z}})\right] \quad (3)$$

Notably, ε_{in} is highly dependent on wavelength. Therefore, the determining factor for the dipole resonance condition of the particle is g_d. That is, when ε_{in} is approximately equal to $-2\varepsilon_{out}$, the electric field is enhanced compared to the incident field. For Ag and Au, this resonance condition occurs for wavelengths in the visible spectrum. Since this resonance condition is the basis for LSPR and the EM field enhancement mechanism for SERS, it is important to describe the dielectric constants that contribute to the plasmon resonance.

Thus far, we have considered the dipole resonance of spherical metal nanoparticles. Although the dipole resonance is most commonly described, it is important to note that higher modes of plasmon excitation (e.g., the quadrupole resonance) are observed. The quadrupole mode arises when half of the electron cloud moves parallel to the applied field and the remainder oscillates antiparallel, an effect that becomes more significant for larger particles [15]. A similar derivation is performed when determining the EM field enhancement of the quadrupole resonance, where the quadrupole polarizability (β) is $\beta = g_q a^5$ and

$$g_q = \frac{\varepsilon_{in} - \varepsilon_{out}}{\varepsilon_{in} + 3/2\varepsilon_{out}} \quad (4)$$

The quadrupole factor (g_q) in **equation 4** demonstrates an extinction dependence on the external dielectric constant, but is less sensitive than the dipole resonance [15]. Although most LSPR sensing experiments detect the changes in dipole resonance, work has demonstrated the dielectric-environment sensitivity of the quadrupole resonance [21]. In this chapter, we restrict the discussion of LSPR to dipole resonances.

3.09.2.1.2 Relationship between the dielectric function and nanoparticle extinction

To fully understand the LSPR resonance condition, it is important to discuss the physical meaning of the dielectric constant. The dielectric constant (ε) or relative permittivity is a dimensionless constant that embodies the electrical behavior of the material in a particular environment compared to vacuum (ε_0). In particular, the dielectric constant describes the behavior of a material when it is immersed in an electric field and is therefore also related to the polarity of the material [22]. The complex dielectric function demonstrates how a material's optical properties are dependent on the incident wavelength of light and can be described by $\varepsilon_{in} = \varepsilon' + i\varepsilon''$, where ε' and ε'' are the real and imaginary dielectric functions, respectively. The real and imaginary components of the dielectric function of a harmonic oscillator can be described by the Lorentz model as (see Ref. [23]):

$$\varepsilon' = 1 + \frac{\omega_p^2(\omega_o^2 - \omega^2)}{(\omega_o^2 - \omega^2)^2 + \gamma^2\omega^2} \quad (5)$$

$$\varepsilon'' = \frac{\omega_p^2 \gamma\omega}{(\omega_o^2 - \omega^2)^2 + \gamma^2\omega^2} \quad (6)$$

In these equations, ω_p is the plasma frequency, ω is the frequency of the incident electric field, ω_o is the natural frequency of the oscillator, taking into account its spring constant and mass, and γ is a damping factor [23]. The plasma frequency is the natural frequency of free electrons and a plasmon is a quantized plasma wave. **Equations 5 and 6** demonstrate the dependence of the dielectric function on the frequency of the incident electric field.

A refinement of the Lorentz model of the dielectric function is the Drude model, valid for conductors that have free electrons. The Drude model is similar to the Lorentz model, but the springs are 'clipped', so that the electrons move about freely [23]. Due to free electron movement, there is no restoring force in this model such that ω_o is zero. In this framework, the equations for the real and imaginary dielectric functions reduce to:

$$\varepsilon' = 1 - \frac{\omega_p^2}{\omega^2 + \gamma^2} \quad (7)$$

$$\varepsilon'' = \frac{\omega_p^2 \gamma}{\omega(\omega^2 + \gamma^2)} \quad (8)$$

Here, the plasma frequency (ω_p) is described by [23]

$$\omega_p^2 = \frac{Ne^2}{m\varepsilon_0} \quad (9)$$

where m is the electron mass, e is the electron charge, and N is the free electron density. If $\omega >> \gamma$, as is common for metals at room temperature, then **equations 7 and 8** are approximated as

$$\varepsilon' \cong 1 - \frac{\omega_p^2}{\omega^2} \quad (10)$$

$$\varepsilon'' \cong \frac{\omega_p^2 \gamma}{\omega^3} \qquad (11)$$

and are identical to the high-frequency limits of the Lorentz model in **equations 5 and 6** [23]. **Equation 9** shows that the square of the plasmon frequency is proportional to the electron density. Therefore, since metals have a particularly high free electron density, the plasmon frequency is likewise high – an observation that has significant consequences for the metal dielectric function [19]. The real part of the dielectric function is approximated by **equation 10** and illustrates that when the plasmon frequency is higher than the frequency of incident light, the ratio of ω_p/ω is greater than 1, leading to a negative real dielectric constant. Therefore, metals have a negative real dielectric constant because they have a high density of free electrons leading to a high plasmon frequency. The negative real dielectric constant resulting from **equation 10** is responsible for resonant Rayleigh scattering and the imaginary dielectric constant is responsible for absorption. Ultimately, these equations demonstrate why the LSPR occurs when an electric field is incident on metals possessing negative real and positive imaginary dielectric constants. As the frequency of the incident electric field changes, so does the complex dielectric function, demonstrating the frequency dependence of the LSPR.

The dielectric function explains the physical basis for the resonance condition, but it is also important to understand how ε_{in} is related to light absorption and scattering of an incident EM field. Here, three possibilities are considered: transmission, scattering, and absorption. When light is transmitted, it has no effect on the particle (and the particle has no effect on the incident field). Scattering results from the acceleration of electrons in the particle that causes them to radiate at the same frequency as the incident wavelength and is often referred to as resonant Rayleigh scattering. Absorption originates from the imaginary component of the dielectric function and occurs when the particle absorbs the incident energy and converts it to other forms of energy (e.g., heat). As mentioned previously, extinction is the sum of absorption and scattering and the corresponding cross-sections are the areas in which these interactions occur. For example, the absorption cross-section describes the area around the particle where incident light is absorbed, often differing from the geometrical cross-section of the particle. The absorption and scattering cross-sections for a small sphere (σ_{abs} and σ_{sca}, respectively) are [15]:

$$\sigma_{abs} = \pi a^2 4x \, \text{Im}(g_d) \qquad (12)$$

$$\sigma_{sca} = \pi a^2 \frac{8}{3} x^4 |g_d|^2 \qquad (13)$$

where $x = (2\pi a \varepsilon_{out}^{1/2})/\lambda$. [15] The cross-sections, as described by **equations 12 and 13** are highly dependent on g_d, further demonstrating its key role in determining the wavelength dependence of scattering and absorption. If the absorption cross-section for a particle is zero, then $\varepsilon'' = 0$. Under this condition, light incident on the particle is solely scattered and/or transmitted.

Incident light on a small spherical particle is transmitted when the imaginary part of the dielectric function is zero and the real part of the dielectric function is positive and equal to the external dielectric. From **equation 10**, this occurs when ω is much higher than ω_p. From the definition of g_d (**equation 2**), when ε' is positive ($\varepsilon'' = 0$), and approaches ε_{out}, g_d and therefore the polarizability become zero, such that there is no extinction and all incident light is transmitted. Alternatively, when ε' is negative ($\varepsilon'' = 0$) and twice the value of ε_{out} in magnitude (i.e., $\varepsilon_{in} = -2\varepsilon_{out}$), g_d approaches infinity and maximum scattering by the spherical particle is observed. Absorption occurs when ε'' is nonzero; that is, the imaginary dielectric function is responsible for light absorption. Because ε_{in} is highly frequency-dependent, the extinction maximum exhibits a corresponding frequency dependence [15]. Examining both **equations 2 and 10** and assuming that the imaginary component of the metal dielectric constant is small, as ε_{out} increases, ε_{in} becomes more negative, which corresponds to a lower incident light frequency that is absorbed or scattered. **Figure 2** shows the real and imaginary dielectric functions of bulk Ag and Al [24]. For Ag, the real dielectric is increasingly negative for longer wavelengths and the imaginary dielectric function is small but positive. Similarly, Al also exhibits a positive imaginary and a negative real dielectric function but in different regions of the spectrum than Ag, suggesting it has different plasmonics properties, which is discussed in section 3.09.4.1. The physical interpretation is the increase in the external dielectric constant damps the frequency of the oscillating surface electrons so they oscillate at lower frequencies; therefore the particle absorbs and scatters longer wavelengths to satisfy the resonance condition.

When the dielectric conditions outlined above are met such that g_d is maximized, a maximum (i.e., referred to as λ_{max}) is observed in the extinction
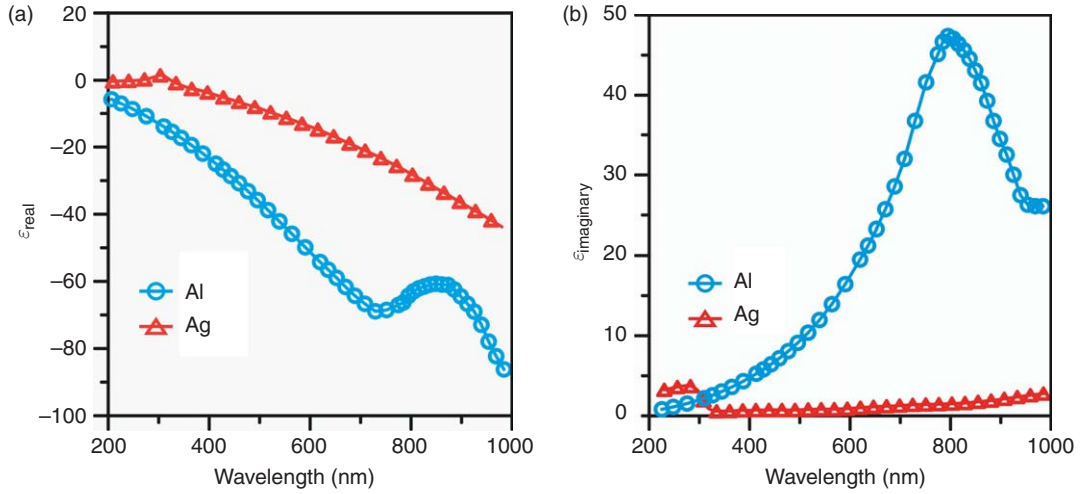
Figure 2 (a) Real and (b) imaginary components of the complex dielectric functions for Ag and Al.

spectrum of the particles. The equation describing the extinction spectrum is derived from Mie's solutions to Maxwell's equations and is as follows [10, 25]:

$$E(\lambda) = \frac{24\pi^2 N a^3 \varepsilon_{out}^{3/2}}{\lambda \ln(10)} \left[\frac{\varepsilon_{in}''(\lambda)}{(\varepsilon_{in}'(\lambda) + \chi\varepsilon_{out})^2 + \varepsilon_{in}''(\lambda)^2} \right] \quad (14)$$

In **equation 14**, $E(\lambda)$ is the wavelength-dependent extinction for spherical metallic nanoparticles, where a is the sphere radius, χ is a shape factor ($\chi = 2$ for a sphere), and N is the number of particles. The shape factor χ is a function of the nanoparticle's aspect ratio and increases proportionally. **Equation 14** also exhibits the impact of the complex dielectric function on the extinction spectrum. When $\varepsilon_{in}' = -2\varepsilon_{out}$ and ε_{in}'' is small and positive, the extinction is maximized. For nonspherical particles, the extinction maximum occurs when $\varepsilon_{in}' = -\chi\varepsilon_{out}$. Thus, for both spherical and nonspherical particles, as ε_{out} changes, a shift in λ_{max} is observed. Therefore, measurements of λ_{max} provide information about the external dielectric environment. The sensitivity of the LSPR λ_{max} to changes in dielectric environment has significant implications for sensing experiments.

3.09.2.1.3 Electric-field decay

The enhanced EM field surrounding metallic nanoparticles is a result of the LSPR. The LSPR of nanoparticles is sensitive to the external dielectric environment in close proximity to the surface. Mie theory is used to examine the distance dependence of the enhanced field, which is approximated to decay

exponentially away from the nanoparticle surface as: $E(z) = E_0 \exp(-z/l_d)$ where l_d is a characteristic decay length [10]. For bulk changes in dielectric environment, such as a solvent or gas, the change in λ_{max} is proportional to change in refractive index (n) of the environment, $\Delta\lambda_{max} = m\Delta n$ [10, 26]. Note that the dielectric constant is the square of the complex refractive index. This equation is valid in situations where the bulk environment extends past the electric field enhancement, such that the electric-field decay lengths are irrelevant. However, for changes in the dielectric environment due to an adsorbate layer, the electric field decay length is important since the adsorbate layer thickness is less than the electric field decay length ($\sim$20 nm). Establishing boundary conditions for the thickness of the adsorbate layer and normalizing the refractive index by the relative field intensity, the following equation is obtained [10, 26]:

$$\Delta\lambda_{max} = m(n_A - n_E)[1 - \exp(-2d/l_d)] \quad (15)$$

where n_A is the refractive index of the adsorbate layer, n_E is the refractive index of the bulk environment, d is the adsorbate layer thickness, and l_d is the decay length of the electric field. A detailed derivation is found elsewhere [10, 26]. When more than one adsorbate layer is present, as is common in many biosensing experiments, additional exponential terms are added to the equation to account for the adsorbate layers occupying different distances in the electric-field decay length. Here it is demonstrated that the effect of the electric-field decay on the sensing capability of the LSPR provides the ability to not only predict λ_{max} shifts with certain adsorbates,

but also to quantify adsorbate layer thicknesses with an observed λ_{max} shift.

3.09.2.1.4 Discrete dipole approximation for nonspherical particles

All discussion thus far has used Mie's exact solutions to Maxwell's equations for spherical particles. Although nonspherical particles are also utilized in LSPR experiments, Mie's solutions still provide an interpretation for nanoparticles that are not necessarily spherical. Because it is usually not possible to solve Maxwell's equations for nonspherical particles analytically, developing numerical methods is important [27]. The discrete dipole approximation (DDA) is a numerically exact method used to describe nonspherical metal nanoparticles and was originally proposed in 1973 [28]. Since DDA is discussed at length in computational chemistry reviews [27], only a brief description is included here. The DDA method divides the particle of interest into a large number of polarizable cubes that interact only through dipole–dipole interactions. The interaction of each dipole with a local electric field induces a polarization that is used to determine the extinction cross-section. Most commonly, the DDA method is used to predict LSPR spectra that provide a comparison with the experimental results from nonspherical nanoparticle extinction experiments. In general, good agreement between computational and experimental results is observed, demonstrating that DDA is an effective numerical method [27].

3.09.2.1.5 Experimental methods

As discussed previously, the extinction of metal nanoparticles is dependent on the wavelength-dependent dielectric function of the metal, the external dielectric environment, as well as the shape and size of the nanoparticles. Typically, nanoparticle extinction is measured using UV–vis spectroscopy in the transmission or reflection geometry. In the transmission geometry, white light is passed through the nanoparticle sample and the light that is not scattered or absorbed is collected by the spectrometer. Again, the maximum of the extinction spectrum is at the wavelength in which g_d is maximized. The reflectance mode is used for samples that have low transmission probability (i.e., reflective surfaces) such that incident light that is not absorbed or scattered is reflected to the spectrometer. In the case of reflectance experiments, the wavelength that satisfies the resonance term is at a minimum in the spectrum. That is, the reflectance minimum is the

extinction maximum. As the external dielectric is changed, the extinction spectrum exhibits measurable changes that demonstrate the sensing capabilities of LSPR spectroscopy.

UV–vis spectroscopy is a relatively simple method of measuring the extinction spectra of metallic nanoparticles. However, this technique is optimal for ensemble-averaged measurements and not single-nanoparticle studies because the shot-noise-governed detection limit is similar to the extinction of a single nanoparticle [29]. Instead, resonant Rayleigh scattering spectroscopy is the most straightforward method for measuring the LSPR of single nanoparticles because the scattering signal is detected above a low background. One example of resonant Rayleigh scattering spectroscopy utilizes dark-field microscopy with a high numerical aperture (NA) dark-field condenser to illuminate the particle and a high-magnification oil-immersion objective with a variable NA to collect only the Rayleigh scattered light [29]. More recently, spatial modulation spectroscopy has enabled measurements of single nanoparticle extinction (i.e., scattering + absorption) [30]. Using these methods, the LSPR of single nanoparticles is measured, enabling careful determination of the structure–property relationships for single nanoparticles.

3.09.2.2 Nanofabrication

3.09.2.2.1 Chemical syntheses

Significant advances in nanofabrication techniques have enabled progress in LSPR spectroscopy. In particular, precise control over the size, shape, heterogeneity, and material composition are critical due to the dependence of LSPR on these properties. Chemical synthetic methods are among the most widely used methods for fabricating large amounts of nanoparticles in solution. For example, Ag colloids formed from the citrate reduction of $AgNO_3$ solution [31] are widely used for LSPR and SERS experiments. Indeed, citrate reduction of a metal is a common method for synthesizing nanoparticles like Ag and Au. Although this method provides a straightforward and quick route to synthesize a large quantity of nanoparticles that support localized surface plasmons, the solution of Ag colloids is quite heterogeneous. The heterogeneity of the Ag colloids is advantageous when a variety of extinction maxima are desired and colloids are easily aggregated using an electrolyte solution (e.g., NaCl). Ag colloid aggregation is an important technique used for SMSERS

[32–34], which is discussed later in the chapter. Although colloidal nanoparticles have a wide variety of applications, a more monodisperse sample is preferred when the LSPR maxima are required to be within a specific range. To circumvent the problem of nanoparticle heterogeneity, researchers have developed techniques to fabricate large amounts of metal nanoparticles in solution that are monodisperse and shape specific (e.g., nanoshells [35], triangular nanoprisms [36], cubes [37, 38], bipyramids [39], and stars [40]). These shape-specific, monodisperse particle syntheses are important for LSPR because they provide a solution of particles with a more homogeneous distribution of LSPR maxima. They also allow for the particle structure to be correlated to the corresponding LSPR spectrum more readily as compared to randomly shaped colloids.

The applications for chemically synthesized nanoparticles range from bulk LSPR measurements to single-nanoparticle LSPR spectroscopy as well as SERS experiments. Single-nanoparticle spectroscopy has proved to be a powerful method to correlate a single particle's structure and LSPR because it removes all of the inherent heterogeneities present in the bulk spectrum. The ability to determine the exact structure that gives rise to a specific LSPR spectrum is quite powerful and particularly important for determining structures that exhibit an optimal SERS enhancement.

3.09.2.2.2 Laser ablation
Chemical syntheses of nanostructures have been widely used for nanoparticles dispersed in solution. However, these methods often require nanoparticle surface stabilizing or functional ligands that are not always necessary or beneficial [41]. Laser ablation synthesis of nanoparticles in solution, pioneered in 1993 [42], is an effective technique that produces nanoparticles without ligands on the nanoparticle surface. Briefly, laser ablation occurs by striking a bulk metal in liquid with a laser, forming a plasma plume that condenses into nanoparticles in solution. Nanoparticles of Au, Ag, and Cu, to name a few, have been synthesized by laser ablation in both aqueous and organic solvents [41]. Although at present, laser ablation does not allow the predetermination of particle size and size distribution, it does allow for the synthesized nanoparticles to be reduced or increased in size by varying laser irradiation. As a relatively new synthetic method for nanoparticles, a complete understanding of the underlying mechanism is still fragmented; however, laser ablation is a promising

approach for the fabrication of nanoparticles in solution without surface ligands. Further research, such as the formation of SERS-active colloids, should increase the utility of nanoparticles formed by laser ablation.

3.09.2.2.3 Nanostructured films
Nanoparticles in solution have a variety of uses and can be drop cast onto a substrate for several experiments. However, some experimental techniques are more straightforward when the nanofabrication occurs on the substrate itself. For example, Ag island films (AgIFs) are created when a thin layer of Ag (6–8 nm) is thermally or electron-beam (e-beam) deposited onto a substrate. The thin layer of Ag is not thick enough to create a continuous film across the substrate and instead forms Ag islands. Because the AgIFs support a surface plasmon and enhance the EM field on the surface, AgIFs have proved to be a simple and fast method to fabricate substrates for SERS [43]. Another nanostructured surface that supports surface plasmons is electrochemically roughened Ag and Au surfaces. Indeed, the substrate in which SERS was first observed in 1974 by Fleischman and coworkers [44] and later described independently by Jeanmaire and Van Duyne [1] as well as Albrecht and Creighton [2] in 1977 was a Ag surface that was roughened electrochemically, illustrating a natural connection between the fields of SERS and electrochemistry.

3.09.2.2.4 Lithographic techniques
Lithographic techniques have provided novel methods for the fabrication of periodic arrays with specific shapes on the nanoscale. These techniques include e-beam lithography, photolithography, and nanosphere lithography (NSL). E-beam lithography is a highly precise method of creating nanoparticles of arbitrary size, shape, and spacing. In this method, an electron beam is used to write a deposition mask directly into a polymer film and metal is then deposited through the mask. The film is removed to leave the remaining nanoparticle pattern on the substrate [10]. E-beam lithography has been used to systematically study the coupling between nanoparticles [45–49] (Section 3.09.2.3.4). Although quite powerful, e-beam lithography is time consuming, expensive, and inefficient for large-scale substrates [10]. Photolithography uses a photo-reactive mask to form arrays of micro- and nanostructures. Specifically, soft lithography utilizes a polymer, such as poly(dimethylsiloxane) (PDMS), as a stamp to transfer patterns fabricated by
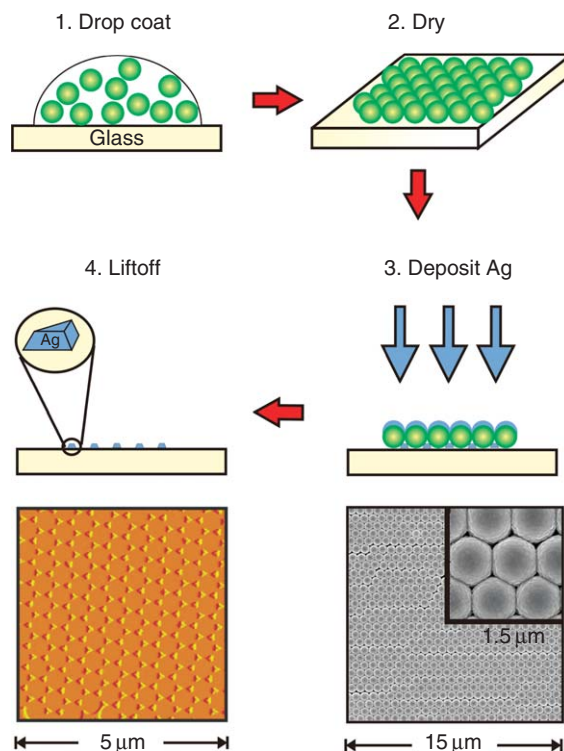
Figure 3   Schematic of NSL for the formation of periodic particle arrays and metal film over nanospheres.

photolithography [50]. These photolithographic methods are diverse and effective for creating patterns of nanostructure arrays of varying complexity and additional information is found elsewhere [50, 51]. A third lithographic technique highlighted here is NSL and in the following paragraphs, the simplicity and versatility of NSL is demonstrated.

NSL, depicted in **Figure 3**, is an extremely valuable and cost-effective technique for generating large two-dimensional (2D) arrays of nanoparticles of a specific shape, size, material, and orientation [52]. The NSL procedure is as follows: polymer or silica nanospheres are drop cast from solution onto a cleaned glass or mica substrate and allowed to dry, self-assembling into a hexagonally close-packed array. From this nanosphere mask, three different routes may be taken. First, between 10 and 100 nm of metal may be deposited onto the nanospheres mask, followed by removal of the nanospheres by sonication. This method produces a periodic particle array (PPA) of metallic nanostructures shaped as truncated tetrahedrons, covering ~7% of the glass substrate [53, 54]. Another route for NSL fabrication is to instead deposit a thicker layer of metal (~200 nm) onto the nanosphere mask to create a

film over nanosphere (FON), as the nanosphere mask is not removed. Metal FONs are widely used for SERS sensing due to the high surface area of the substrate. A third approach is to subject the nanosphere mask to reactive-ion etching through the nanosphere mask generating wells between the spheres [55]. The metal is then deposited over the nanospheres and into the wells. The spherical mask is removed, and nanoparticles remain anchored to the glass substrate. Reactive-ion etching provides a unique NSL-fabricated structure because the nanoparticles are rod shaped.

In addition to FONs and PPAs, NSL is used to fabricate alternative nanoparticle structures. Typically, the nanosphere mask is a monolayer and produces truncated tetrahedron shaped PPAs; however, when a double nanosphere mask layer is used, hexagonally shaped particles are formed after metal deposition [54]. Additionally, by changing the metal deposition angle, new shapes may be fabricated [53, 54]. The variety of sizes and shapes of nanoparticles fabricated by NSL is important as it demonstrates the wide versatility of the technique. Moreover, NSL-fabricated nanoparticles may also be released into solution. To this end, NSL was used to fabricate particles on a substrate that were functionalized

with a self-assembled monolayer (SAM) to prevent nanoparticle aggregation and then released into solution by sonication [56, 57]. The SAM was present on all sides of the nanoparticle except for the base that was attached to the glass substrate. Next, a dithiol was added to the solution to link two nanoparticles together. The monomers and dimers were characterized using UV–vis spectroscopy, atomic force microscopy (AFM), transmission electron microscopy (TEM), and computational methods, and the particles exhibited distinct LSPR spectra on a substrate, in solution, and as dimers.

Overall, NSL is a cost-effective and high-throughput method to fabricate nanoparticle arrays. The ability to easily vary the size and shape of the nanoparticles produces a highly tunable LSPR extinction maximum that is discussed in the following section. NSL is also indifferent to the type of metal and by using a variety of metals like Ag, Au, Al, and Cu its applications can be further expanded.
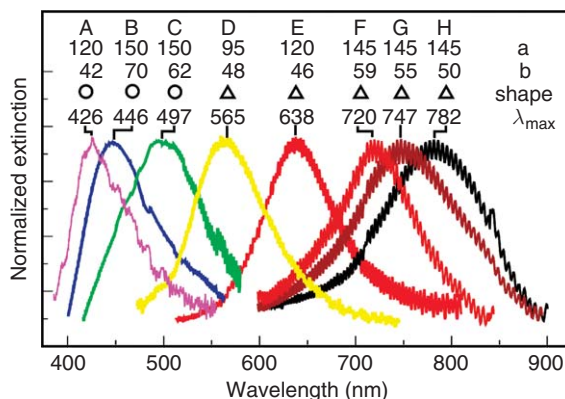
3.09.2.3 Characteristics of the LSPR

#### 3.09.2.3.1 Dependence on nanoparticle size and shape

According to Mie theory, the LSPR of a nanoparticle is highly dependent on its size and shape. Therefore, by fabricating nanostructures with varying sizes and shapes, the LSPR can be tuned to a distinct wavelength. For example, Ag triangles, spheres, rods, cubes, and stars exhibit unique LSPR spectra because of their differing size and shape. NSL-fabricated nanoparticles are particularly useful for demonstrating the relationships between nanoparticle size and shape and LSPR. That is, the LSPR is sensitive to

shape changes in the in-plane and out-of-plane directions, which can be varied independently using NSL. Figure 4 displays the tunability of the LSPR extinction maximum across the visible range of the spectrum for a Ag PPA [53]. Increasing the in-plane nanoparticle width, a (by increasing the size of the nanospheres used in the mask), results in a shift towards lower-energy wavelengths. Increasing the out-of-plane height, b, of the nanoparticles shifts the LSPR toward higher-energy wavelengths. Therefore, varying these size parameters alone can produce a distribution of LSPR maxima. However, the LSPR is also dependent on the shape of the nanoparticles. Without any further modification, the shapes of the nanoparticles fabricated by NSL are truncated tetrahedrons. However, by thermal annealing, the truncated tetrahedrons are transformed into hemispheres. Generally, these hemispheres have LSPR extinction spectra at shorter frequencies than a truncated tetrahedron fabricated with similar parameters (Figure 4) [53].

As described above, the size and shape dependence of NSL-fabricated Ag nanoparticles can be systematically studied by varying the nanosphere size and metal thickness. Another method to vary nanoparticle size and shape is achieved by electrochemical modification. NSL particle arrays fabricated on indium tin oxide, a transparent conducting surface, were used for simultaneous optical and chronocoulometry measurements [58]. The controlled particle shape, size, and interparticle spacing of these arrays make them ideal candidates to monitor (1) the electrochemical modification of the nanoparticle structure and (2) the LSPR shifts resulting from the changing structure. The results are

	A	B	C	D	E	F	G	H	
	120	150	150	95	120	145	145	145	a
	42	70	62	48	46	59	55	50	b
	○	○	○	△	△	△	△	△	shape
	426	446	497	565	638	720	747	782	λ_{max}

Figure 4   Modification to the LSPR maximum of periodic particle arrays with changing nanoparticle (a) in-plane width and (b) out-of-plane height.
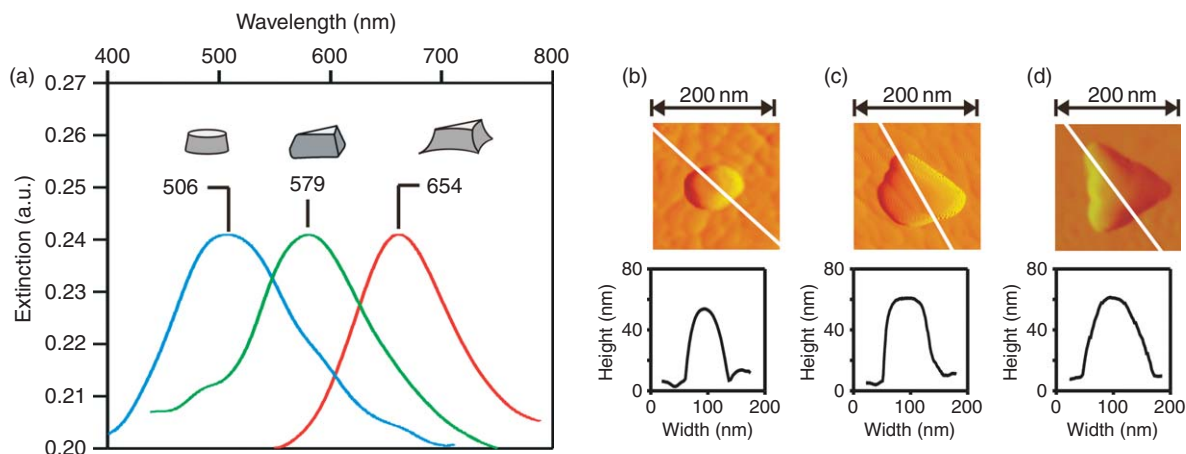
Figure 5   Electrochemical modification of Ag nanoparticles on indium tin oxide measured by (a) LSPR and (b–d) AFM.

displayed in **Figure 5**. As the Ag particles are oxidized, the shape is changed, as exhibited by scanning electron microscopy (SEM) and AFM, and the LSPR spectrum is shifted. These experiments illustrated that the particles were preferentially oxidized first at the bottom edges, next at the triangular tips, and finally the out-of-plane height. In these correlated studies, the relationship between the nanoparticle in-plane width and the LSPR maximum could be studied systematically, because the out-of-plane height does not change during the first several chronocoulometric runs. This spectroelectrochemical study demonstrated a quantitative manipulation of Ag nanoparticle geometries along with spectral monitoring [58]. The Mie theory predicts the nanoparticle size and shape dependence of the LSPR and NSL has proved to be a cost-effective, controlled experimental demonstration of this dependence.

3.09.2.3.2   Sensitivity to external environment

The LSPR is extremely sensitive to the environment surrounding the particle. That is, the frequency of the conduction electrons' oscillation is highly dependent on the external dielectric constant, which is related to the refractive index. The dependence of LSPR on ε_{out} can be separated into two general regimes, the bulk environment and the local environment. The bulk environment typically refers to the entire area surrounding the nanoparticle, such as air or solvent. Shifts in the LSPR extinction maximum are proportional to the change in refractive index when switching from one environment to another, demonstrated by the expression $\Delta\lambda = m\Delta n$. The refractive-index sensitivity of the nanoparticles'

LSPR was demonstrated by exposing the NSL-fabricated Ag nanoparticles to N_2 and different solvents, which have different refractive indices. A plot of the change in λ_{max} versus refractive index, n, for a variety of solvents is displayed in **Figure 6(a)**, demonstrating a linear relationship between $\Delta\lambda_{max}$ and n, where the slope of this line is the refractive-index sensitivity, m [59]. **Figure 6(a)** also shows the variation of refractive-index sensitivity with different sizes of NSL-fabricated nanoparticles, where the particle arrays with the shortest out-of-plane height have the highest sensitivity. Overall, the typical refractive-index unit (RIU) sensitivity for NSL-fabricated particles is 200 nm RIU^{-1}. In other words, a change of about 0.005 RIU produces an LSPR λ_{max} shift of 1 nm. Ultimately, experiments aimed at elucidating the refractive-index sensitivity of LSPR play a critical role for the development of biosensing applications.

Refractive-index studies were repeated on SAM-functionalized Ag PPAs [60]. Thiolated SAMs are ideal since they are available with a variety of terminal functional groups, and thiols chemisorb easily to both Ag and Au. **Figure 6(b)** displays the LSPR peak shift as a function of the surrounding medium's refractive index for both unmodified (line A) and hexadecanethiol (HDT)-modified (line B) Ag nanoparticles. It can be seen that the unmodified particles have a higher refractive-index sensitivity (191 nm RIU^{-1}) compared to the HDT-modified particles (150 nm RIU^{-1}). This observation is not surprising, considering that the EM field decays away from the particle surface. The presence of the HDT monolayer diminishes the sensitivity to external environments by ~20%, as the strongest sensing capabilities occur closest to the nanoparticle surface
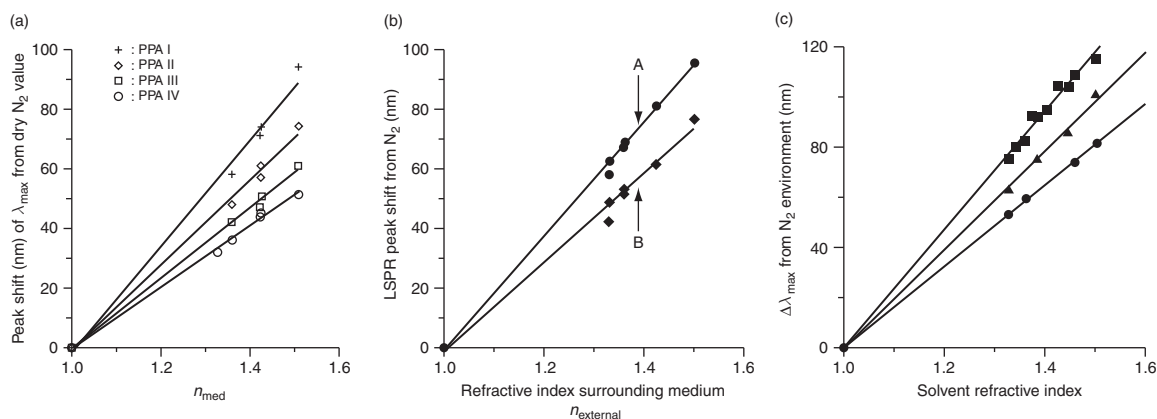
Figure 6 Refractive-index sensitivity of the LSPR spectra for Ag nanoparticles with (a) different sizes, (b) an adsorbate layer, or (c) for individual nanoparticles of various shapes.

where the HDT monolayer resides. Although the overall sensitivity of the SAM-modified PPA is decreased relative to the bare PPA, it is important to note that bulk solvent-induced shifts are readily observed and detected, indicating that the EM field extends far enough away from the particle surface to be useful for sensing experiments. Another significant result from this experiment is that an HDT monolayer produces a 40-nm LSPR shift relative to a bare PPA. An observation with important implications for sensing experiments is that this 40-nm shift corresponds to just 100 zmol of HDT. When an adsorbate layer is present, **equation 15** is used for determining the LSPR shift and is also used to estimate the surface coverage of adsorbates or the adsorbate thickness from the LSPR shift. Ultimately, the sensing experiments that examine bulk and adsorbate refractive-index changes using NSL-fabricated particle arrays provide fundamental information for future work, including single-nanoparticle sensing.

Measurements of single nanoparticles have several benefits to ensemble-averaged measurements. First, single nanoparticles are readily implemented in multiplexed detection schemes, since each unique nanoparticle possesses a distinguishable LSPR maximum. An additional advantage is that the absolute detection limit (number of analyte molecules per nanoparticle) is significantly reduced. A third advantage of single-nanoparticle spectroscopy is the ability to measure the LSPR spectrum of individual particles with a high signal-to-noise ratio [29]. Overall, the advantages of single nanoparticle spectroscopy provided motivation to examine the environmental dependence of single nanoparticle LSPR [29, 61].

The following experiments utilized resonant Rayleigh scattering spectroscopy to demonstrate the LSPR λ_{max} response of individual Ag nanoparticles to varying solvent environments and the formation of a monolayer of small-molecule adsorbates [29].

The refractive-index sensitivity of individual Ag nanoparticles was measured by exposing the nanoparticles to various solvent environments and single nanoparticles with three different shapes were used to illustrate the effect of nanoparticle shape on refractive-index sensitivity [29]. The nanoparticle shapes were inferred from TEM imaging [62], LSPR line shape, LSPR λ_{max}, and LSPR polarization dependence. Similar to the results from ensemble-averaged measurements, the LSPR λ_{max} is shifted to longer wavelengths as the refractive index of the solvent is increased, as displayed in **Figure 6(c)**. The particle with the largest aspect ratio (a rod-shaped particle) exhibited the highest refractive-index sensitivity, consistent with predictions from Mie theory. The refractive-index sensitivity decreased with decreasing particle aspect ratio. These single-nanoparticle studies exhibited the adsorption of fewer than 60 000 HDT molecules on a single Ag nanoparticle resulting in an LSPR shift of 40.7 nm, thus demonstrating low-zeptomole sensitivity [29]. Overall, current research on single-nanoparticle LSPR suggests a promising future for single-nanoparticle sensing experiments.

Significant work has focused on developing the adsorbate sensing capabilities of LSPR biosensors using both nanoparticle arrays and single nanoparticles. For example, researchers have utilized nanoparticle arrays to successfully detect and sense concanavalin A binding to a monosaccharide [12], electrostatic

binding of poly-L-lysine to carboxylic acid-terminated SAM-modified Ag nanoparticles [60], avidin binding to biotinylated Ag particles [63], antibiotin binding to biotinylated Ag particles [64], Alzheimer's disease biomarkers [65, 66], and most recently, the calcium-induced conformational changes of calmodulin [13]. Single-nanoparticle LSPR spectroscopy has demonstrated biomarker detection on cancer cells *in vitro* [67]. Readers are directed to recent reviews for a survey of plasmonic biosensors [11, 68–70]. The sensing capabilities of nanoparticles have been examined by bulk and adsorbate refractive-index studies on both particle arrays and single nanoparticles.

3.09.2.3.3 Distance dependence

Two important consequences of the LSPR are: (1) the enhanced EM field at the surface of the nanoparticle and (2) an environmentally sensitive extinction spectrum. These consequences are understood by using a model for the refractive-index response, depicted in **equation 15,** demonstrating the change in extinction maximum is a function of refractive-index, adsorbate layer thickness, and decay length of the EM field. Although this model assumes a single exponential decay of the EM field (accurate for propagating plasmons) [10, 26, 71], which is an oversimplification for localized surface plasmons, it accurately describes the sensor's distance dependence by the adsorbate thickness, d, and EM-field decay length, l_d. Unfortunately, the equation alone does not provide nanoparticle structural information that is directly related to the refractive-index sensitivity.

In order to characterize the relationship between structure and sensitivity as well as characterize the EM-field decay, long- [72] and short-term [73] distance-dependence experiments were performed using SAMs and multilayers (layers of carboxylic terminated thiols alternating with Cu^{2+} ions). However, these studies were limited by the unknown variability in the refractive index of an SAM and a low resolution layer thickness. To better characterize the distance and structural sensitivity dependence of LSPR, a high-resolution distance-dependence study was performed using ALD, which provides atomic resolution and an extremely uniform refractive-index layer. Using ALD, up to 600 single layers (1.1 Å each) of Al_2O_3 were deposited onto Ag nanoparticle arrays and the LSPR was observed [71]. The LSPR shift with increasing Al_2O_3 film thickness is shown in **Figure 7**. Notably, an LSPR shift is apparent after a single 1.1 Å layer of Al_2O_3, demonstrating
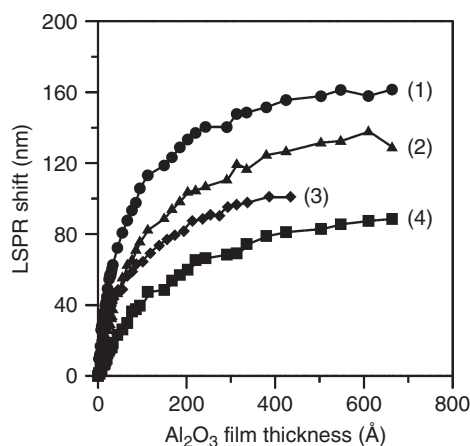
Figure 7 Observed LSPR shift from Ag nanoparticles of various shapes and sizes (1–4) as a function of Al_2O_3 film thickness.

excellent sensitivity to the local environment. Additionally, **Figure 7** shows the variability of sensitivity as the nanoparticle structure is changed: lines 1, 2, and 4 represent truncated tetrahedral-shaped particles with in-plane widths of 90 nm and out-of-plane heights of 30, 40, and 51 nm, respectively. Line 3 represents hemispherically shaped particles with in-plane width of 104 nm and out-of-plane height of 52 nm. As the out-of-plane height of the nanoparticles is increased, the refractive-index sensitivity of the particles is decreased, demonstrating a relatively modest LSPR shift. Although the different nanoparticles exhibit varying refractive-index sensitivities, for all cases (lines 1–4) the slope of the LSPR shift versus Al_2O_3 thickness is decreased as additional Al_2O_3 layers are deposited, as expected due to the EM-field decay away from the nanoparticle surface [71]. These distance-dependence studies are important for understanding the EM-field decay from the nanoparticle, an important consideration for SERS sensing experiments.

3.09.2.3.4 Coupling among nanoparticles

The LSPR studies presented thus far have examined bulk solutions of nanoparticles, nanoparticle arrays, or single nanoparticles. However, it is well known that the LSPR of metallic nanoparticles is dependent on other surrounding nanoparticles and, therefore, in this section the coupling between nanoparticles is examined. Nanoparticle coupling is a significant area of research because nanoscale devices comprised of assemblies or arrays of nanoparticles are greatly affected by the interactions between nanoparticles [45]. The extent

of coupling can be examined by measuring changes to the LSPR maximum that occur when the interparticle spacing is varied [45, 74, 75].

The dependence of the LSPR on interparticle coupling was demonstrated by examining the LSPR shift of Ag and Au nanoparticles in varying array arrangements [45]. For Au and Ag nanoparticle arrays fabricated by e-beam lithography, the LSPR shift to shorter wavelengths when the lattice spacing of the array is decreased. Slight differences in LSPR shifting behavior were observed between nanoparticles in square or hexagonal arrays, consistent with differences in lattice density, such that denser lattices have a relatively high-energy LSPR. Blue shifts are observed when relatively large lattice spacing (i.e., approximately $\lambda_{max}/2$) is decreased due to radiative dipole interactions between nanoparticles. When the lattice spacing is small (<100 nm), the LSPR is shifted to longer wavelengths for Au nanoparticles [76]. Overall, this work provides an example of the LSPR dependence on particle spacing in an array and highlights the sensitivity of the LSPR to neighboring nanoparticles.

3.09.2.4 Functionalization and Stabilization of Nanoparticles

Functionalization of plasmonic nanostructures is sometimes necessary for LSPR and SERS sensing, specifically for analytes with low or no affinity to noble metals. In addition to the use of SAMs, surface modification can be achieved with ALD. ALD is a thin-film growth technique based on the alternating use of self-terminating reactions between gaseous precursor molecules and a substrate [77]. One advantage of ALD over other vapor deposition methods is the precise thickness control afforded by the self-limiting nature of the surface reactions. Film growth proceeds in a layer-by-layer fashion and coats even high-aspect-ratio and porous structures with extreme uniformity. The reaction sequence for the ALD of Al_2O_3 from trimethylaluminum (TMA) and water, one of the most commonly used ALD processes, is as follows [78]:

(A) $Al\text{-}OH^* + Al(CH_3)_3 \rightarrow Al\text{-}O\text{-}Al(CH_3)_2{}^* + CH_4$
(B) $Al\text{-}CH_3{}^* + H_2O \rightarrow Al\text{-}OH^* + CH_4$
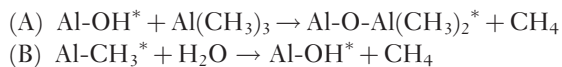
In schemes A and B the asterisks represent surface species and the reactions are simplified to show only a single functional group. One AB sequence is referred to as a cycle, and thickness is simply controlled by the number of cycles. The growth of Al_2O_3

has been shown to proceed at a rate of $\sim$1 Å per cycle [71, 79]. It is important to note that, because SERS intensity falls off with increasing distance from the surface, the ability to grow films with subnanometer thickness is highly desirable to minimize signal losses. Moreover, the wide variety of inorganic materials that can be grown by ALD presents new possibilities for versatile surface functionalization.

Metal oxides such as Al_2O_3 also serve to protect Ag surfaces from oxidation, thus increasing the robustness of SERS substrates. In fact, coating Ag nanoparticles with very thin Al_2O_3 films by ALD results in substrates that are also vastly more stable when exposed to high temperatures, laser excitation, and solvent environments [80, 81]. The structural integrity of SERS nanostructures can be probed by imaging techniques such as AFM and SEM. Alternatively, changes to nanoparticle structure can be interrogated by monitoring the LSPR extinction spectrum. The sensitivity of the LSPR to size and shape highlighted earlier in this chapter enables the detection of even slight shape changes that are not observable by AFM or SEM [80].

3.09.2.4.1 Thermal stability
At high temperatures, the tips of triangular Ag nanoparticles become rounded, eventually annealing into hemispheres, an energetically more favorable geometry. Previous work has indicated that hemispherically shaped nanoparticles exhibit smaller EM enhancement relative to triangular Ag nanoparticles [82]. These substrates, therefore, have been limited to SERS studies conducted at ambient temperatures. For certain applications, such as the study of catalytic reactions that often occur at high temperatures, the development of thermally robust SERS substrates is a necessary requirement. It has been shown that very thin Al_2O_3 layers deposited by ALD over Ag SERS substrates fabricated by NSL provide significant protection against thermal annealing [81]. LSPR spectroscopy and SEM were used to monitor the stability of Ag nanoparticles having a 0.2–1.0 nm layer of Al_2O_3 at various temperatures. SEM images revealed that after 1 h at 300°C in N_2, bare triangular Ag nanoparticles turned into hemispheres, whereas nanoparticles coated with just 0.2 nm Al_2O_3 maintained their original shape (**Figures 8(a) and 8(b)**). The plasmon resonance of bare Ag nanoparticles at 500°C under N_2 for 1 h were blue-shifted by 192 nm, while the plasmon resonance of Ag nanoparticles having 1.0 nm of Al_2O_3 shifted just 16 nm. In addition, Al_2O_3-coated nanoparticles
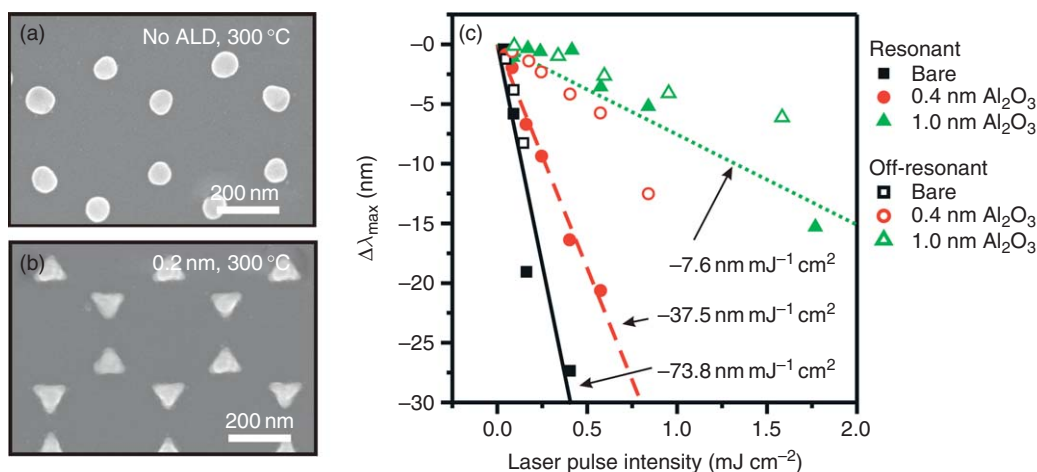
Figure 8 Modifications to Ag nanoparticle shape for bare and Al_2O_3-coated structures upon (a, b) thermal annealing and (c) exposure to laser pulses of different energies monitored by SEM and LSPR spectroscopy.

were found to be stable at $500\,°C$ over the course of 6 hours. These results indicate that ultrathin layers of Al_2O_3 are an effective means of stabilizing SERS substrates for use at high temperatures.

3.09.2.4.2 Stability to laser excitation

For surface-enhanced nonlinear spectroscopy, high laser intensity is often required to achieve sufficient signal. However, metal nanoparticles are susceptible to melting or deformation caused by the high-power ultrashort laser pulses that are commonly used in nonlinear spectroscopy. Modifications to nanoparticle shape in bare and Al_2O_3-coated Ag nanoparticles upon exposure to laser pulses of varying intensity in both resonant and off-resonant conditions were monitored using LSPR spectroscopy [80]. **Figure 8(c)** shows the shift in LSPR λ_{max} for bare Ag nanoparticles and nanoparticles with 0.4 and 1.0 nm of Al_2O_3, for resonant and off-resonant conditions. For each laser pulse intensity, bare nanoparticles exhibited the largest LSPR shift and nanoparticles with 1.0 nm Al_2O_3 exhibited the smallest LSPR shift. For all cases, the shift in LSPR λ_{max} increased with increasing laser pulse intensity, showing an approximately linear relationship. The slopes of these linear fits reveal that a 1.0 nm layer of Al_2O_3 provides a factor-of-10 improvement in the stability of Ag nanoparticles. This enhanced stability is attributed to the increased surface melting temperature resulting from the decreased mean square displacement of Ag atoms located on the nanoparticle surface. Consequently, Al_2O_3-coated silver nanoparticles can serve as a

stable platform for both linear and nonlinear ultrafast surface-enhanced laser spectroscopy.

3.09.2.4.3 Solvent stability

Exposure to organic solvents or aqueous solutions results in structural changes to unmodified triangular Ag nanoparticles fabricated by NSL which in turn affect their optical properties [60]. Specifically, the tips of the nanoparticles become rounded, resulting in a blue shift in the LSPR spectrum. Similar solvent-induced morphology changes have also been observed for other SERS substrates, such as thin Ag films [83]. The stability of Al_2O_3-coated SERS substrates has been explored in various solvent environments, which is critical for liquid-phase studies. For Ag nanoparticle arrays fabricated by NSL, the LSPR was monitored as a function of time for 2 h in each of eight different solvents having a range of refractive indices and polarities. The extent of structural changes induced by solvent exposure depended on the particular solvent. In each case, however, NSL-fabricated Ag nanoparticles coated with ~2 nm of Al_2O_3 were significantly more protected against these solvent-induced structural changes. In the case of Ag film over nanospheres (AgFONs), Al_2O_3 coatings as thin as 4 Å prevent surface oxidation and delamination of the Ag film upon exposure to water. For catalytic applications, the use of ALD to coat Ag SERS substrates with ultrathin Al_2O_3 layers thus enables the study of surface reactions in catalytically relevant liquids like water, ethanol, and methanol at elevated reaction temperatures using SERS.

3.09.3 Surface-Enhanced Raman Spectroscopy

3.09.3.1 Background

In 1928, Raman and Krishnan observed that monochromatic light incident on molecules resulted in normal Rayleigh scattering as well as modified scattered radiation of different frequencies [84]. The energies of this modified radiation corresponded to the characteristic frequencies of molecular vibrations. Therefore, Raman spectroscopy, as it was later termed, provides the unique vibrational signature of molecules. In the classical picture of Raman scattering, the incident EM field induces a dipole moment in the molecule, which in turn radiates light at its oscillation frequencies. The induced dipole moment, μ_{ind}, is described by $\mu_{ind} = \alpha E_0$, where E_0 is the applied field and α is the polarizability of molecule. The induced dipole moment may radiate at several frequencies: (1) ω, the frequency of the incident light (Rayleigh scattering), (2) ω-ω_{vib}, where ω_{vib} is the frequency of a normal mode vibration (Stokes Raman scattering), and (3) ω+ω_{vib} (anti-Stokes Raman scattering). The intensity of Raman scattering scales as ω^4 and is proportional to the square of the polarizability derivative, $(\delta\alpha/\delta Q)^2$, where Q is the normal nuclear mode of the molecule [85]. Therefore, Raman scattering occurs only if the applied field induces a polarizability change along the nuclear mode. Although Raman spectroscopy is a powerful technique for probing the vibrational modes of molecules, it suffers from poor sensitivity due to the inherent weakness of the scattering process. Raman cross-sections are small ($\sim 10^{-29}$–10^{-3} cm^2 molecule^{-1}) in comparison to typical absorption cross-sections ($\sim 10^{-15}$–10^{-16} cm^2 molecule^{-1}). Therefore, for 10^{10} incident photons, only about 1 photon will be Raman scattered.

Given the weakness of the Raman effect, detecting Raman scattering from a monolayer of adsorbed molecules on a surface would be extremely difficult. For this reason, the original observation of surface Raman signal from pyridine on electrochemically roughened Ag [44] was quite remarkable. It was soon realized that the Raman signal of pyridine was enhanced by a factor of $\sim 10^6$ [1, 2], implying huge enhancement due to a surface effect. Because the induced dipole involved in Raman scattering is the product of the molecular polarizability and the applied electric field, it follows that enhancement of Raman intensity would arise from an increase in one of these factors. Thus, chemical (CHEM) and EM mechanisms were proposed to account for surface-enhanced Raman scattering. Since the discovery of SERS, researchers have devoted much effort to understanding the relative contributions of the CHEM and EM mechanisms to the overall SERS EF. In general, it is now understood that the dominant effect is EM enhancement ($\sim 10^4$–10^8, depending on the nanostructure) resulting from excitation of the LSPR, while CHEM enhancement may account for a factor $\leq 10^2$. Strong experimental proof of the existence and magnitude of the CHEM mechanism, however, has not been well established.

3.09.3.1.1 Chemical enhancement mechanism of SERS

CHEM enhancement is postulated to arise from direct interaction between the adsorbed molecule and the metal surface, resulting in an increase in the Raman cross-section for the adsorbed molecule relative to the solution phase [86, 87]. Chemisorption, or bond formation between the molecule and the surface, perturbs the electronic structure and therefore the optical properties of the molecule compared to its unbound state. One way in which the Raman cross-section may be affected by electronic effects is through charge transfer between the adsorbed molecule and the surface [88–90]. Specifically, interaction between the molecular orbitals of the adsorbate and the electronic band structure of the metal allows for transfer of electrons between the molecule and the metal surface. CHEM enhancement, therefore, involves new or altered electronic states that become accessible as a result of chemisorption. If the absorbance maximum of an adsorbed molecule is altered such that it is closer to the laser excitation frequency, the cross-section of the molecule is increased. Thus, the CHEM mechanism can be understood as a type of resonance Raman effect. Evidence for the CHEM mechanism was observed in early electrochemical experiments in which enhancement was observed to vary, depending on the applied potential [91–93]. Since the electrode potential affects the Fermi level of the metal, charge transfer between the adsorbate and the electrode surface changes with applied potential. Further evidence for the CHEM mechanism was provided by the observation that SERS intensities of CO and N_2 differ by a factor of 200 under the same experimental conditions [86, 94]. This result cannot be explained using the EM mechanism in which enhancement is not molecule specific, but rather a property of the substrate.

Ultimately, the requirement for direct adsorbate–surface interaction dictates that the CHEM enhancement mechanism is a short-range effect, limited to only the first layer of adsorbed molecules.

3.09.3.1.2   *Electromagnetic enhancement mechanism of SERS*

To describe the EM mechanism of SERS, we return to the simple model of EM radiation incident on a spherical metal particle that is smaller than the wavelength of light. Recall from the earlier discussion of LSPR theory that the electric field surrounding this particle is given by **equation 1**. Since the complex dielectric function of the metal is strongly wavelength dependent, the magnitude of enhancement is likewise wavelength dependent. Note that the field enhancement decays as r^{-3}, suggesting a finite sensing volume surrounding the nanoparticle. The nature of the excitation wavelength and distance dependence of SERS will be explored in more detail in Section 3.09.3.2.

Since the intensity of Raman scattered light is proportional to $E_0{}^2$, which is greatly enhanced at the nanoparticle surface, the Raman intensity therefore depends on the absolute square of E_{out}, evaluated at the nanoparticle surface ($r = a$). From **equation 1**, where $\alpha = g_d\, a^3$, this is given for a small metal sphere by:

$$|E_{out}|^2 = E_0{}^2 \left[|1-g|^2 + 3\cos^2\theta\left(2\mathrm{Re}(g) + |g|^2\right)\right] \quad (16)$$

where θ is the angle between the incident field vector and the vector which describes the position of the molecule on the surface. The largest field enhancements are obtained for $\theta = 0°$ or $180°$, where the molecule is aligned along the polarization direction. When g is large, the maximum enhancement approaches $|E_{out}|^2 = 4E_0{}^2|g|^2$. The field intensity as a function of position for a spherical Ag nanoparticle is shown in **Figure 9**. The maximum field intensity on a metal sphere differs from the minimum field intensity by a factor of 4, and the radially averaged intensity is $|E_{out}|^2 = 2E_0{}^2|g|^2$.

The overall physical picture of EM enhancement in SERS that emerges from this simple model is as follows. When a molecule adsorbed to the surface of a metal nanoparticle is irradiated with light, an oscillating dipole in the molecule is created which is enhanced by the metal substrate. The resulting radiation is decreased in energy by an amount equal to the vibrational frequencies of the molecule (i.e., Stokes Raman). In addition to
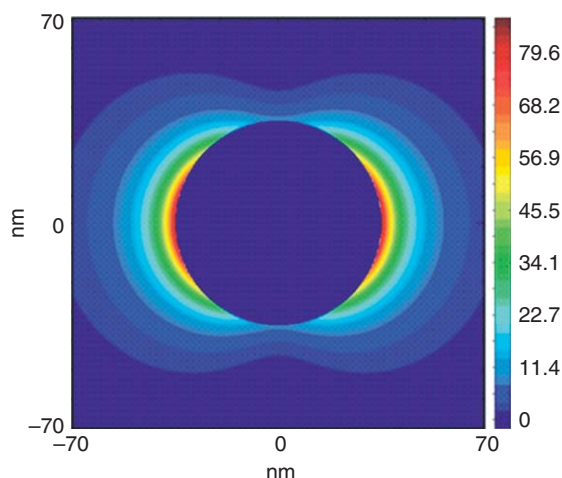
Figure 9   Calculated electric field intensity $\left(|E_{out}|^2\right)$ around a spherical Ag nanoparticle.

enhancement of the incident field expressed in **equation 16**, enhancement of the emitted light from the induced dipole is also possible. Because the emitted field is not constant over the volume of the sphere as is the incident field, this enhancement is more complicated to evaluate. A rigorous treatment of enhanced emission is given by Kerker and coworkers [95, 96]. To a first-order approximation, the enhanced emission can also be modeled using **equation 16** simply by replacing the excitation frequency with the Raman Stokes-shifted frequency. Therefore, the overall EF from both incident and scattered fields can be described as

$$EF = \frac{|E_{out}|^2|E'_{out}|^2}{|E_0|^4} = 4|g|^2|g'|^2 \quad (17)$$

where the primed symbols refer to fields evaluated at the scattered frequency. This expression describes the theoretical EF resulting from the EM mechanism of SERS. If the Stokes shift is small, then g and g' are evaluated at approximately the same wavelength such that the EF scales as g^4. This relationship is the origin of the 'E^4 enhancement' commonly referred to in the SERS literature. The derived EF expression matches exactly the results of Kerker's more rigorous approach, supporting the validity of the approximations used for this model. For a small sphere with $|g| \sim 10$, the resulting EM EF is $\sim 10^4$–10^5. EM enhancements are actually rather small for spherical nanoparticles because their

plasmon resonance condition is met near the UV region of the spectrum where damping due to metal interband transitions is more prevalent. Therefore, the magnitude of $|g|$ can be much larger for prolate spheroidal objects and nanoparticles of higher-order structure (e.g., aggregates).

3.09.3.1.3   Calculating SERS enhancement factors

While the EM EF can be predicted theoretically, the overall SERS EF (i.e., enhancement due to both CHEM and EM mechanisms) is calculated experimentally by measuring both the SERS and normal Raman spectroscopy (NRS) signals of a given analyte. The scattering intensity in NRS is given by the following expression:

$$I_{NRS} = K(v) \times N_{NRS} \times \frac{\partial \sigma}{\partial \Omega} \times I_{0,NRS} \times v^4 \times t_{NRS} \quad (18)$$

where $K(\nu)$ is the instrument response function, N_{NRS} is the number of molecules within the probe volume, $\frac{\partial \sigma}{\partial \Omega}$ is the differential Raman cross-section of the molecule, $I_{0,NRS}$ is the laser intensity, ν^4 is the frequency dependence of the scattering process, and t_{NRS} is the acquisition time. SER scattering intensity is analogous to that measured in NRS but is multiplied by a factor due to surface enhancement, expressed as EF_{SERS}:

$$I_{SERS} = K(v) \times N_{SERS} \times \frac{\partial \sigma}{\partial \Omega} \times I_{0,SERS} \times v^4 \times t_{SERS}$$
$$\times EF_{SERS} \quad (19)$$

The comparison of I_{SERS} and I_{NRS} is greatly simplified if the collection geometry is similar and the same excitation frequency is used, such that $K(\nu)$ and ν^4 are constant. When the intensities are normalized for laser power and acquisition time, the ratio of the two intensities can be rearranged as

$$EF = \frac{I_{SERS}/N_{SERS}}{I_{NRS}/N_{NRS}} \quad (20)$$

This expression describes the overall enhancement in Raman scattering that is observed for molecules in close proximity to the surface of a plasmonic nanostructure. The SERS EF can therefore be calculated from the normalized SER and NR intensities of a given analyte and the number of molecules interrogated in each measurement. In practice, however, determining the number of molecules that give rise to Raman and SER signal is quite challenging.

For example, the SERS EF for benzenethiol on a Ag nanoparticle array fabricated by NSL was calculated by comparison of the intensity of the 1575 cm^{-1} mode with the corresponding peak measured from solution [97]. The SER spectrum of benzenethiol ($\lambda_{ex} = 670$ nm) on a Ag nanoparticle array is shown in **Figure 10(a)**. The surface-enhanced 1575 cm^{-1} peak intensity is 22.9 ADU s^{-1} mW^{-1} (I_{SERS}). The NR spectrum of benzenethiol in a 37 µm-thick cell at the same excitation wavelength is shown in **Figure 10(b)**. The 1575 cm^{-1} peak intensity from the NR measurement is 0.792 ADU s^{-1} mW^{-1} (I_{NRS}). To estimate the number of molecules probed in a SERS measurement, the laser spot size, surface area of the substrate, and surface coverage of the molecules must be known. In this experiment, the beam waist of the objective used was determined to be 4.0 µm by a scanning silicon knife edge test. Assuming a monolayer of benzenethiol on the surface of a Ag nanoparticle array with a packing density of 6.8×10^{14} molecules cm^{-2} and ~7 % surface coverage of the nanoparticles, approximately 6.3×10^6 molecules are probed in the SERS measurement (N_{SERS}). For the NR experiment, the number of molecules within the probe volume, approximated as a cylinder with a radius of 2.0 µm and a height of 37 µm, was 2.7×10^{12} molecules (N_{NRS}). Substitution of the N_{SERS} and N_{NRS} values along with intensities from the normalized SER and NR spectra into the above equation give an SERS EF of 1.24×10^7.
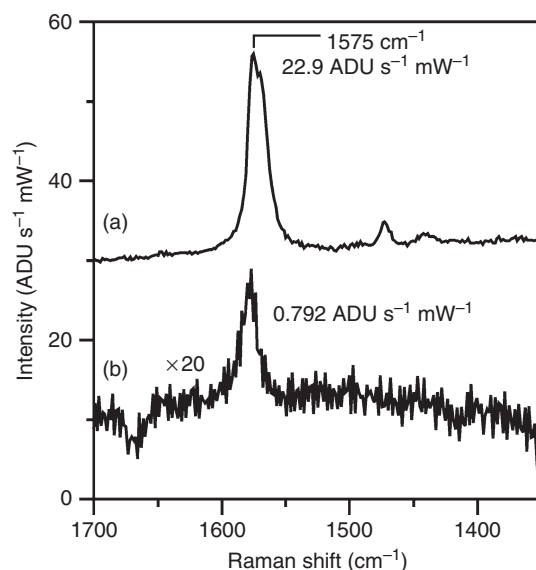
Figure 10 Calculating the enhancement factor for benzenethiol on a Ag nanoparticle array: comparison of (a) SER and (b) normal Raman spectra of benzenethiol ($\lambda_{ex} = 670$ nm).

3.09.3.2   Experimental Consequences of the EM Mechansim

3.09.3.2.1   Distance dependence of SERS

An important consequence of the EM mechanism is that the adsorbate is not required to be in direct contact with the surface. Enhanced EM fields generated by excitation of the LSPR extend beyond the surface of the substrate, thereby creating a volume within a few nanometers of the surface in which molecules are detected. The long-range effect predicted by the EM mechanism differs from the CHEM enhancement mechanism, which requires that molecules be directly chemisorbed to the surface. For the practical application of SERS, the ability to detect molecules near the surface, but not necessarily bound to it, is crucial since many analytes have low or no affinity to Ag or Au. In such cases, specificity for the analyte can be improved by modifying the surface with overlayers. The field enhancement around a small metal sphere decays with r^{-3}, and given the E^4 enhancement, SERS intensity should therefore scale with r^{-12}. However, at increased distances from the nanoparticle, the surface area is also increased, scaling as r^2, which leads to an overall SERS distance dependence of r^{-10}:

$$I_{SERS} = \left(\frac{a+r}{a}\right)^{-10} \tag{21}$$

where I_{SERS} is the intensity of a particular Raman mode, a is the average size of the field-enhancing features on the surface, and r is the distance from the surface to the adsorbate [98].

To probe the distance dependence of SERS, the SER spectrum of pyridine was measured at increasing distances from an AgFON surface modified with ultrathin Al_2O_3 layers of various thicknesses deposited by ALD (**Figure 11(a)**) [99]. The relative intensity of the $1594\ cm^{-1}$ mode as a function of Al_2O_3 thickness is shown in **Figure 11(b)**. By fitting the experimental data to **equation 21,** the average size of the enhancing feature, a, was found to be 12.0 nm. The surface-to-molecule distance at which the SERS intensity is decreased by a factor of 10, d_{10}, for this substrate is 2.8 nm. However, this value was derived assuming a complete monolayer of Al_2O_3 was formed for each ALD cycle, but quartz crystal microbalance measurements indicate the average growth rate for Al_2O_3 on Ag is ~1.1 Å per cycle [71]. Thus, the value of d_{10} could be as low as 1.0 nm. Overall, these results clearly demonstrate that SERS is a long-range effect, in agreement with the predictions of the EM mechanism.

3.09.3.2.2   Excitation-wavelength dependence of SERS

According to the EM mechanism, the maximum SERS signal is predicted to occur when both the
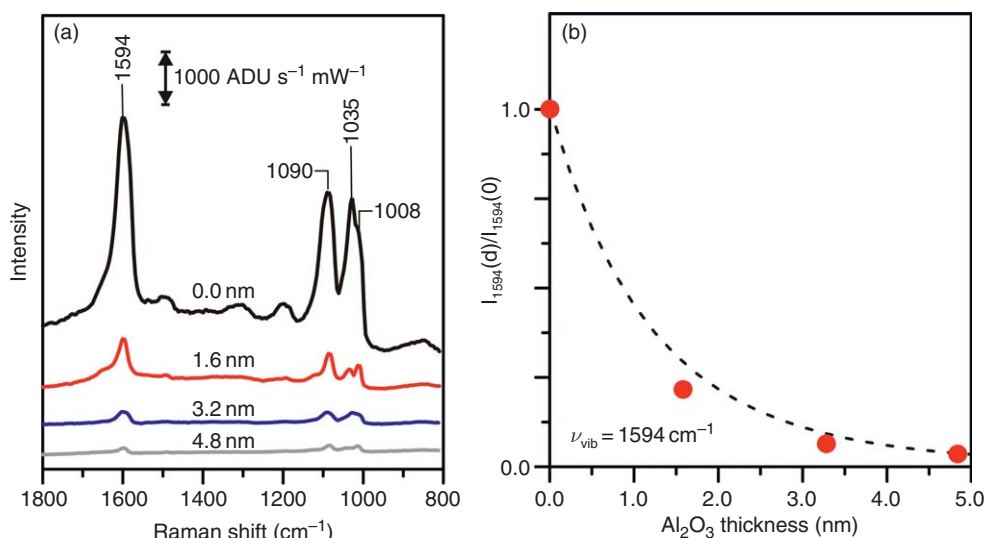
Figure 11   Distance dependence of SERS: (a) SER spectra of pyridine measured at increasing distances from an AgFON surface modified with ultrathin Al_2O_3 layers of various thickness and (b) relative intensity of the $1594\ cm^{-1}$ mode as a function of Al_2O_3 thickness.

incident and scattered photons are strongly enhanced at the metal surface. It was recognized early on that wavelength-scanned surface-enhanced Raman excitation spectroscopy (WS SERES), in which SERS enhancement is measured at several excitation wavelengths, could be used to probe this effect. Unfortunately, early experiments were limited by fixed-frequency laser sources resulting in low data point density or limited spectral coverage [100–102]. The use of a broadly tunable laser system with a versatile detection system enabled the first detailed WS SERES experiments [97]. In particular, WS SERES profiles were measured for benzenethiol adsorbed to Ag nanoparticles fabricated by NSL. The narrow size distribution of these Ag nanoparticle arrays results in a well-defined LSPR that can be precisely tuned throughout the visible and NIR regions.

WS SERES profiles were measured for excitation wavelengths in the range of 420–500, 532–690, 532–740, and 630–800 nm for Ag nanoparticle arrays having an LSPR λ_{max} at 489, 663, 699, and 810 nm,

respectively, and plotted for the 1575 cm^{-1} mode of benzenethiol. An important detail is that the relevant LSPR extinction spectra correspond to the LSPR measured after adsorption of the analyte, which is red-shifted relative to the LSPR of the bare substrate. To account for variations in intensity unrelated to enhancement by the substrate, SER spectra were corrected using the NR signal from neat cyclohexane ($\nu = 1444$ cm^{-1}) as an intensity standard. The WS SERES profiles exhibited line shapes similar to the extinction spectrum of the substrate, and were fit to Gaussian functions. In each case, the maximum SERS enhancement was observed for excitation wavelengths slightly higher in energy than the LSPR λ_{max}, with the difference in energy corresponding to roughly half the vibrational frequency of the Raman mode. To generalize the magnitude of this energy difference, the WS SERES profiles for three different vibrational modes of benzenethiol (1575, 1081, and 1009 cm^{-1}) were compared for a single substrate (**Figure 12**). The difference in energy between the LSPR λ_{max} and the peak excitation
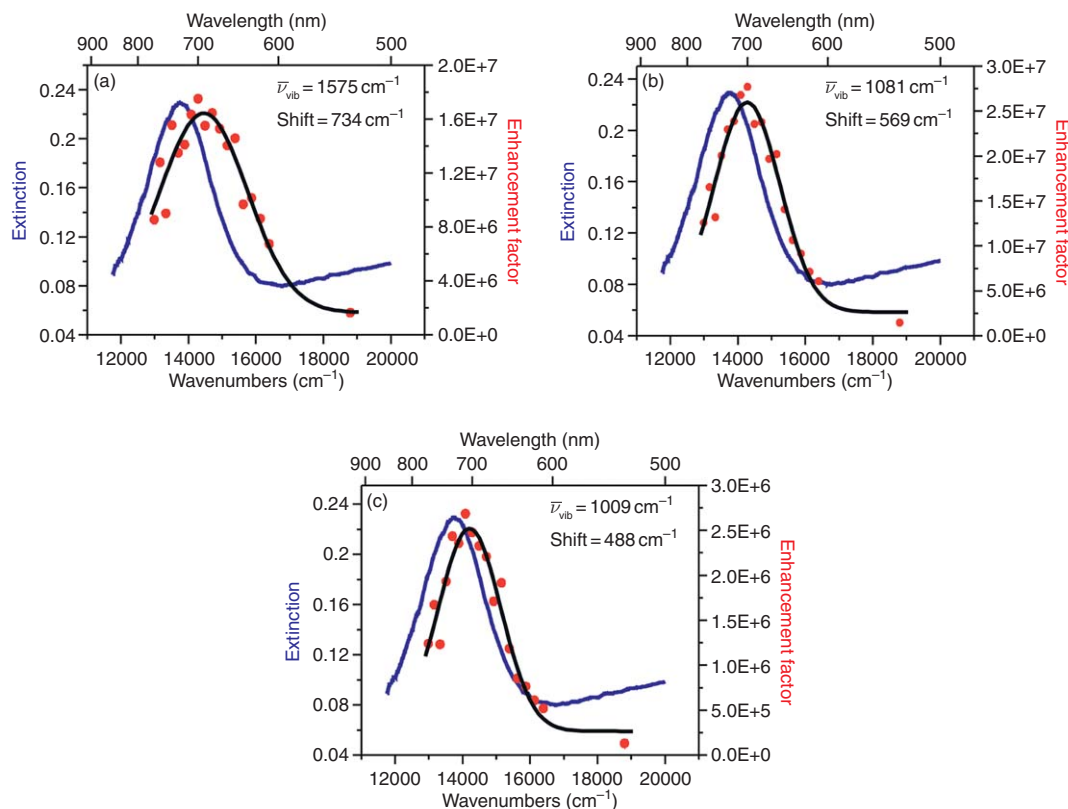
Figure 12 Wavelength-scanned SER excitation profiles and LSPR spectra measured for benzenethiol adsorbed to Ag nanoparticles fabricated by NSL.

frequency was found to increase with increasing vibrational mode frequency. For all three modes, the magnitude of the separation was approximately half the Raman frequency. Therefore, maximum SERS enhancement occurs when the LSPR λ_{max} is located between the peak excitation frequency and the vibrational frequency, wherein both incident and scattered photons are enhanced by the LSPR. In addition to supporting the fundamental EM mechanism of SERS, these experiments also highlight the practical importance of optimizing both the plasmon and excitation frequencies in order to achieve the maximum SERS enhancements for any application.

3.09.3.2.3   Excitation-wavelength dependence of SERRS

When a resonant Raman scatterer is adsorbed to a SERS-active surface, the relationship between the LSPR of the substrate and the frequency dependence of surface-enhanced resonant Raman spectroscopy (SERRS) is more complex owing to coupling between the molecular resonance and the plasmon resonance. Previous studies have demonstrated that when resonant molecules are adsorbed to nanoparticles, the magnitude of the observed LSPR shift depends strongly on the spectral overlap between the plasmon resonance of the nanoparticles and the molecular resonance of the adsorbed species [103–106]. In order to explore the impact of this coupling on SERRS signal as a function of excitation frequency, wavelength-scanned surface-enhanced resonance Raman excitation spectroscopy (WS SERRES) profiles were measured on Ag nanoparticle arrays fabricated by NSL [107]. The probe molecule for this study, Tris(2,2′-bipyridine)-ruthenium (II) ($Ru(bpy)_3^{2+}$), has an absorbance maximum at 452 nm and a shoulder at 425 nm corresponding to a metal-to-ligand charge-transfer transition. In order to ensure monolayer coverage on the Ag nanoparticles, the surface coverage of $Ru(bpy)_3^{2+}$ on a Ag electrode was determined using double potential step chronocoulometry. It was found that an incubation time of 30 min in 0.1 mM $Ru(bpy)_3^{2+}$ yielded monolayer coverage on the Ag surface ($\sim 0.65 \times 10^{14}$ molecules cm^{-2}). The LSPR shift induced by adsorption of a monolayer of $Ru(bpy)_3^{2+}$ on Ag was then measured for Ag nanoparticles with various LSPR λ_{max}. For Ag nanoparticles with λ_{max} blue of the $Ru(bpy)_3^{2+}$ resonance, the LSPR shifted by $\sim$20 nm. However, the LSPR shift was dramatically decreased to just 5 nm when the λ_{max} was very close to the $Ru(bpy)_3^{2+}$ resonance. As λ_{max} was tuned to be slightly red of the $Ru(bpy)_3^{2+}$ resonance (453 nm),

an amplified LSPR shift of 50 nm was observed. Finally, as the λ_{max} was moved further red of the $Ru(bpy)_3^{2+}$ resonance, the LSPR shift was decreased to $\sim$15 nm. Overall, the sharp increase in LSPR shift from 5 to 50 nm that occurs within 10 nm of the molecular resonance is consistent with predictions by quasi-static electrodynamics modeling and previous observations for other resonant molecules [103, 106, 108].

WS SERRES profiles of $Ru(bpy)_3^{2+}$ on three different Ag nanoparticle arrays were measured for excitation wavelengths in the range of 400–500 nm for substrates with an LSPR λ_{max} at 434.7, 465.2, and 480.1 nm. Excitation profiles for both the 1487 and 1602 cm^{-1} modes of $Ru(bpy)_3^{2+}$ were fit to Gaussian functions (**Figure 13**). The observed trends in surface enhancement versus excitation wavelength differ from the nonresonant case, in which the greatest enhancement consistently occurred when the excitation wavelength was slightly blue-shifted from the LSPR λ_{max} of the adsorbate-covered substrate. This deviation is attributed to coupling of the molecular electronic resonance with both the laser excitation frequency (resonance Raman effect) and the LSPR frequency. In particular, the WS SERRES profiles for the 1487 cm^{-1} mode appear to be biased toward the $Ru(bpy)_3^{2+}$ electronic absorption, whereas data for the 1602 cm^{-1} mode more closely resemble nonresonant behavior. An examination of SERR spectra taken at different excitation energies reveals that when excitation energy near the molecular resonance was used (457.9 nm), the 1487 to 1602 cm^{-1} mode intensity ratio is 2.5. However, when the excitation frequency was moved away from the molecular resonance to higher energy (420 nm), this ratio changed to 1.2. Thus, the 1487 cm^{-1} mode is more resonantly enhanced relative to the 1602 cm^{-1} mode. To better understand the relationship between the LSPR, molecular resonance, and the WS SERRES profile, a theoretical model based on multiplication of EM and resonance enhancement mechanisms was proposed. The resonance enhancement profile of $Ru(bpy)_3^{2+}$ was approximated to have the same shape as the molecular absorbance, with a maximum resonance enhancement of 40 (based on the known value for $Fe(bpy)_3^{2+}$, an analog of $Ru(bpy)_3^{2+}$). When the resonant EF was multiplied by the theoretical EM enhancement for $Ru(bpy)_3^{2+}$, the predicted profiles were in good agreement with the observed experimental trends. Ultimately, the results of the WS SERRES experiment with $Ru(bpy)_3^{2+}$ are consistent with an overall enhancement that involves multiplicative EM and resonance Raman contributions.
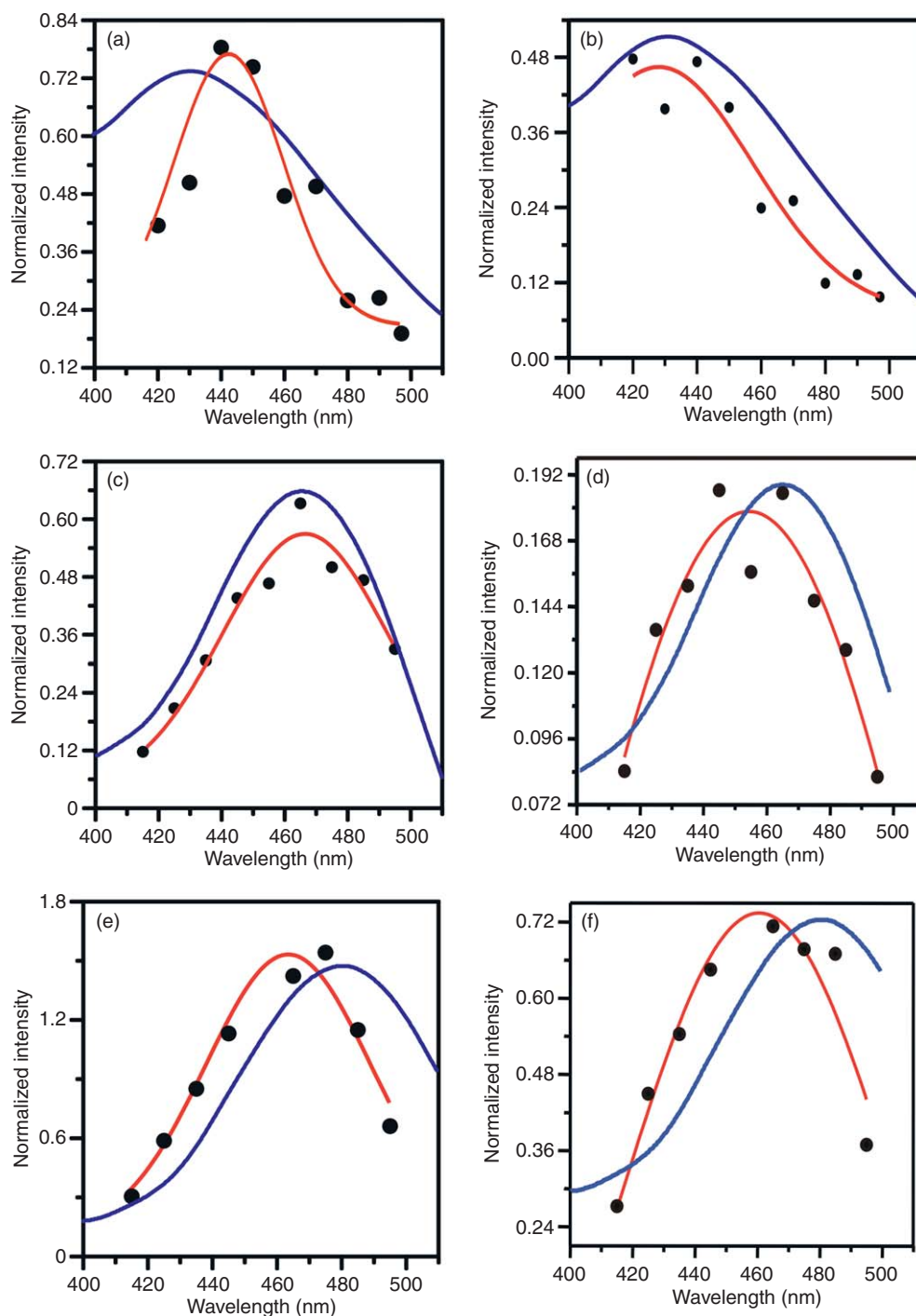
Figure 13 LSPR spectra and wavelength-scanned SERR excitation profiles measured for (a), (c), and (e) the 1487 cm^{-1} peak and (b), (d), and (f) 1602 cm^{-1} peak of Ru(bpy)$_3$$^{2+}$ on three different Ag nanoparticle arrays.

3.09.3.3 Single-Molecule SERS

The observation of surface-enhanced Raman spectra from individual molecules was independently reported in 1997 by the groups of Nie [4] and Kneipp [3]. Nie and Emory observed Raman scattering from single rhodamine 6G (R6G) molecules

adsorbed on Ag nanoparticles at concentrations corresponding to zero or one analyte molecule per nanoparticle ($<10^{-10}$ M) [4]. The observations of polarization sensitivity and changes in the position and intensity of vibrational bands as a function of time suggested single-molecule behavior. Kneipp *et al.* observed SMSERS of crystal violet on Ag nanoparticles in solution. The signal intensity was quantized and corresponded to 0, 1, 2, and 3 molecules in the probe volume, and the probability of observing *n* molecules followed the Poisson distribution [3]. Given the low number of photons scattered in a typical Raman experiment ($\sim 10^{-4}$ photons s^{-1} molecule^{-1}), the detection of inelastic scattering from a single molecule is remarkable, and the initial reports of SMSERS immediately generated substantial interest. Subsequently, researchers sought a definitive proof that Raman signal originates from just one molecule. Evaluation of SMSERS based on temporal fluctuation in signal intensity, or blinking, was shown to be an unreliable proof of single-molecule detection [109]. Problems associated with the use of Poisson statistics corresponding to quantized intensities have also been discussed [110, 111].

In addition to SMSERS focused on fluctuation in the intensity domain, the observation of competing analytes in SMSER spectra provided further evidence for single-molecule behavior. In particular, Doering and Nie [112] noted spectral interchange between R6G and the citrate background (present from the synthesis of Ag nanoparticles), suggesting that blinking in SMSERS is due to surface diffusion in the proximity of a hot spot, or region of very high EM enhancement. Competitive adsorption between two analytes, R6G and benzotriazole, was then used by Etchegoin and coworkers to verify single-molecule activity [113, 114]. However, interpretation of results based on the bi-analyte approach is complicated due to differences in Raman cross-section, absorption spectra, and surface binding affinity of the two analytes [110].

3.09.3.3.1   *A frequency domain existence proof of SMSERS*

Building upon the concept of the bi-analyte approach, an isotopologue approach was developed in which two isotopologues of R6G, R6G-d_0 (non-deuterated) and R6G-d_4 (deuterated), were used to prove single-molecule activity [32]. Isotope editing circumvents the problems associated with the bi-analyte technique since isotopic substitution does not significantly alter the electronic absorbance, surface chemistry, or Raman cross-section of the molecule. However, the vibrational bands associated with C-D stretching and bending will shift in frequency relative to C-H bands, resulting in a unique vibrational signature for each molecule. Single-molecule behavior can therefore be verified by tracking the spectral signature of analyte molecules adsorbed at sufficiently low concentrations. When two isotopologues are introduced to a solution of Ag nanoparticles such that, on average, only one type of molecule is adsorbed to each nanoparticle aggregate, most SMSER spectra display the spectral features of a single isotopologue.

The SER spectra from 50 individual nanoparticle aggregates were acquired under a dry N_2 environment from randomly chosen active sites identified by dark-field scattering. **Figure 14(a)** displays representative spectra from two of the spots measured, which clearly indicate the presence of only one isotopologue within each probe volume. Analyte assignment was based on the sole presence of the 622 or 610 cm^{-1} mode, characteristic of only R6G-d_0 or R6G-d_4, respectively. Of the 50 spots sampled, 24 had solely R6G-d_4 character, 22 had solely R6G-d_0 character, and four showed character from both isotopologues, as shown by the histogram in **Figure 14(b)**. The overall probability of measuring either isotopologue follows a combined Poisson–binomial distribution, providing strong evidence of single-molecule detection. Histograms of the peak location in the 600 cm^{-1} region for the single-molecule events fit to Gaussian functions with a full width at half-maximum (FWHM) of 3.0 and 4.8 cm^{-1} for R6G-d$_4$ and R6G-d_0, respectively, illustrate the degree of spectral wandering observed. Spectral wandering in SMSERS is significantly greater than spectral fluctuation due to instrument instability, measured to be 0.6 cm^{-1} for the 1028.3 cm^{-1} NR mode of cyclohexane. For the ensemble-averaged spectra of R6G-d$_4$ and R6G-d_0, the corresponding FWHM were 5.3 and 6.9 cm^{-1}, respectively. Therefore, the distribution of vibrational frequencies hidden by the ensemble average can be elucidated by SMSERS. This work clearly demonstrates that the ensemble-averaged spectrum is a superposition of single-molecule states. The isotopologue and bi-analyte approaches have emerged as the most definitive proofs for single-molecule detection in SMSERS to date. Indeed, it is anticipated that the isotopologue approach in particular will have substantial impact on future SMSERS experiments.
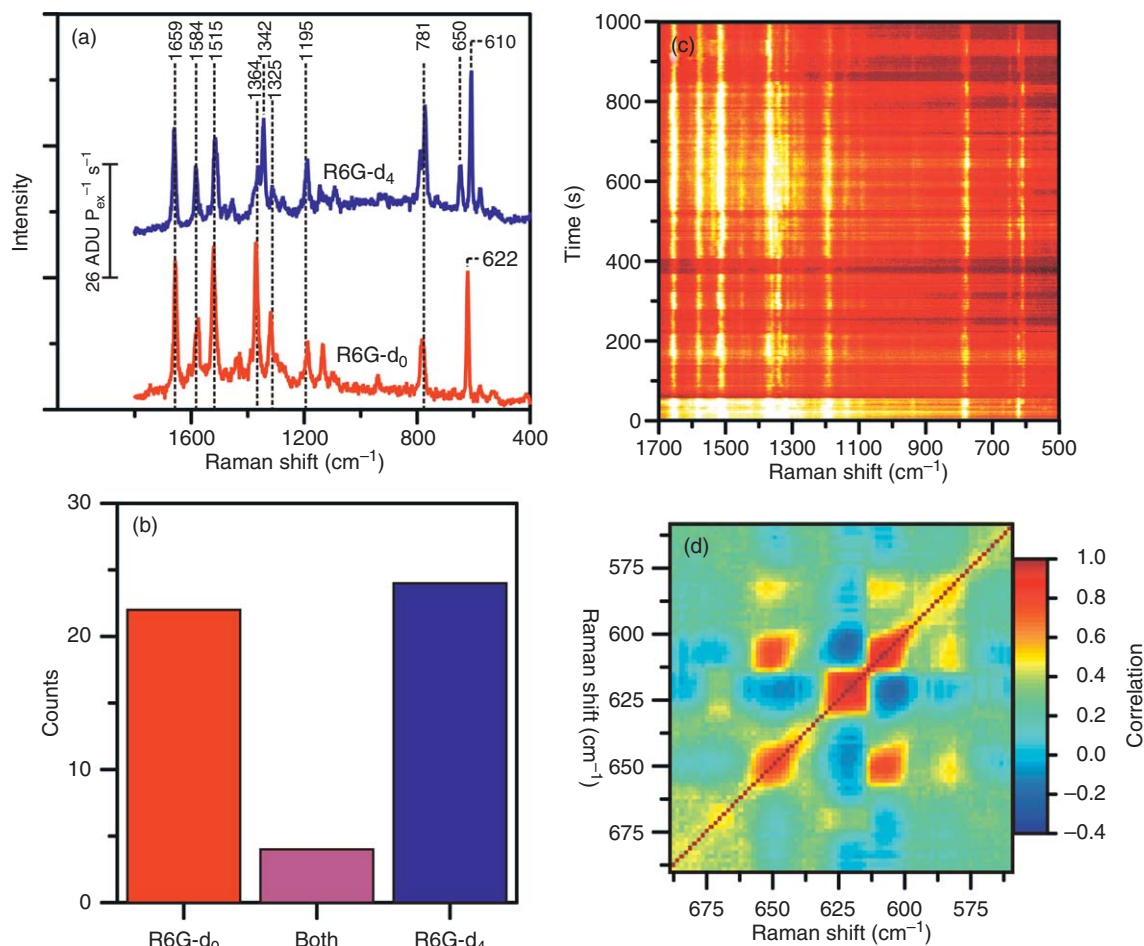
Figure 14 (a) Representative single-molecule SER spectra for R6G isotopologues and (b) corresponding histogram of deuterated, nondeuterated, or both-molecule events. (c) Waterfall plot of SER intensity versus time under ambient conditions showing surface dynamics and (d) corresponding cross-correlation of dynamic switching demonstrating the analytes compete for the same hot spot.

3.09.3.3.2 Surface dynamics in SMSERS

The effect of the nanoparticle environment on SMSERS was also investigated for the R6G/Ag system [32]. In a dry N_2 environment no blinking was observed, but under ambient conditions, and for higher coverages of R6G on Ag (statistically, ~50 R6G-d_0 and 50 R6G-d_4 molecules adsorbed per nanoparticle aggregate), surface dynamics were observed. A waterfall plot of Raman scattering as a function of time is displayed in **Figure 14(c)**. At $t = 0\,s$, only the characteristic vibrational signature of R6G-d_0 is observed, which is unexpected given the higher concentration of molecules on the surface. Furthermore, the integrated intensity is similar to that seen in the single-molecule experiment described earlier, indicating that the signal is

originating from only one molecule rather than the 100 molecules in the ensemble. This suggests that the EF in the hot spot is actually three to four orders of magnitude greater than the average EF for the nanoparticle, in agreement with previous results [3, 4]. Over the course of 1000 s, the spectrum switches completely from R6G-d_0 to R6G-d_4 and back to R6G-d_0, displaying dynamic behavior.

Given that SMSERS nanoparticle aggregates may contain more than one hot spot, two explanations for the observed switching behavior are possible: (1) two or more molecules are competing for the same hot spot on the surface, or (2) two or more molecules are acting independently at two different hot spots within the same probe volume. By analyzing the data with 2D cross-correlation [115] it is possible to

differentiate between these cases. For two different hot spots in close proximity, the dynamic behavior of the molecules over time should be noncorrelated ($\chi = 0$). If, however, the two molecules compete for the same hot spot, their behavior should be anticorrelated ($\chi = -1$). The 2D cross-correlation of the time evolution data (**Figure 14(d)**) demonstrates strong correlation ($\chi = 0.8$) between the two vibrational bands characteristic of R6G-d_4 (650 and 610 cm^{-1}). In addition, the vibrational bands associated with the cross-peaks between R6G-d_0 and R6G-d_4 display anticorrelation ($\chi = -0.3$). In 2D cross-correlation analysis, a strong correlation of the Stokes band to the continuous SERS background is observed, such that even in the absence of a peak there is some time-correlated background contribution [116]. The correlation ($\chi = 0.2-0.4$) that remains between the background and the characteristic frequencies of the molecule is consistent with this observation. As a result, the magnitude of the anticorrelation is in fact even larger than the measured value. The results of 2D cross-correlation analysis therefore point to the existence of only one active hot spot in the probe volume, with molecules moving in close proximity to it.

3.09.3.3.3   Structure and enhancement factors of SMSERS hot spots

Most SMSERS studies to date have been conducted on colloidal Ag nanoparticles. It is well established that these Ag nanoparticles are extremely heterogeneous, with only a small fraction that exhibit SMSERS activity [112]. The lack of substrates having well-defined structures and reproducible single-

molecule activity is a current limitation to the broad application of SMSERS. Moreover, characterizing the nature of SMSERS-active sites is also necessary to understand the underlying mechanisms. Structural determinations of SMSERS-active sites by AFM and polarization-modulation measurements suggested that 'hot' particles result from the aggregation of two or more Ag nanoparticles [4, 117, 118]. These studies led to the notion that molecules were in fact adsorbed to 'hot spots', or regions of high EM enhancement located between adjacent particles.

High-resolution TEM (HRTEM) images with correlated optical spectra of SMSERS-active nanoparticle structures and electrodynamics calculations provide further evidence for EM hot spots in nanoparticle aggregates [34]. The TEM images of nanostructures with confirmed single-molecule activity consisted of nanoparticle dimers as well as higher-order aggregates. No SMSERS active structures consisting of a single Ag nanoparticle were observed, suggesting that two or more particles are necessary for single-molecule activity. The Ag nanoparticle dimer in **Figure 15(a)**, the simplest single-molecule structure observed to date, can be approximated as a hemispherically capped rod and a sphere arranged in a T-shaped geometry. Electrodynamics calculations using the DDA with this structure as input confirm that SMSERS hot spots occur near the particle–particle junction with enhancements on the order of ~10^8 (**Figure 15(b)**), consistent with the combination of molecular resonance and EM field enhancement. Importantly, this detailed study of the specific nanostructures that give rise to SMSERS suggests that simple nanoparticle dimers can be used for the rational design of SMSERS substrates.
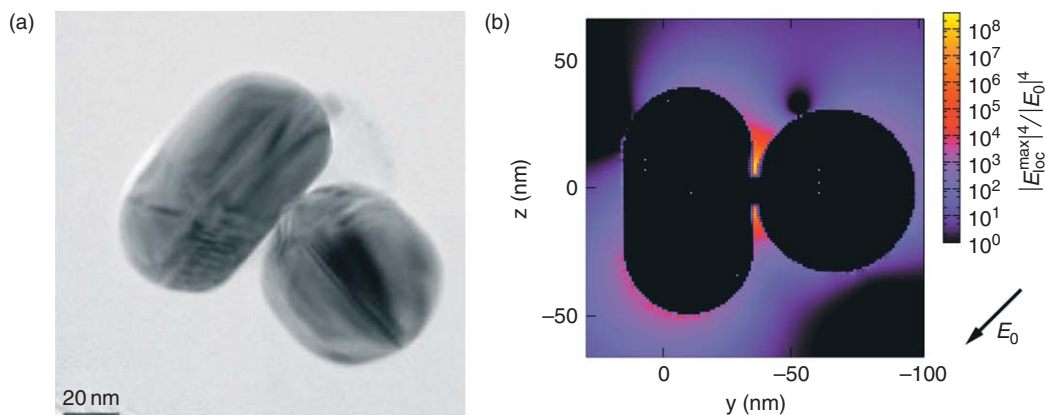

Figure 15   (a) High-resolution transmission electron micrograph of an SMSERS-active Ag nanoparticle aggregate and (b) corresponding EM enhancement map calculated with DDA.

In addition to structural characterization, substantial attention has been devoted to understanding the large enhancements that arise from SMSERS hot spots. Original estimates of the enhancement from SMSERS-active sites were $\sim 10^{14-15}$, based on a typical Raman scattering cross-section ($\sim 10^{-30}$ cm^2) [3, 4]. However, the (resonance) Raman cross-section of R6G was determined to be $\sim 10^{-23}$ cm^2, based on femtosecond stimulated Raman spectroscopy measurements [119]. This implies that resonance effects account for as much as 10^7 of the reported 10^{14-15} EFs for R6G on Ag. The remaining $\sim 10^8$ enhancement can be attributed to surface effects, which is in agreement with the DDA calculations for the EM EF of the SMSERS-active structure discussed above. Both experimental and theoretical data, therefore, support the view that SMSERS sensitivity results from multiplication of the surface plasmon excitation and resonance Raman enhancement.

3.09.3.3.4   Excitation-wavelength dependence of SMSERS

While progress has been made in characterizing the structure of SMSERS hot spots and it is now known that EFs of $\sim 10^8$ can support single-molecule signal, many fundamental mechanistic questions remain. The relative contributions of the EM, CHEM, and resonance Raman enhancements to single-molecule sensitivity are of particular interest. Specifically, the contributions of resonance Raman versus surface effects when excitation occurs far from the molecular resonance are not well understood. Previous SMSERS studies of R6G on Ag have employed various excitation wavelengths. The SER spectra of R6G at five different excitation wavelengths (λ_{ex} = 632.8, 532.0, 514.4, 488.0, and 457.9 nm) were measured, where maximum sensitivity ($\sim 10^{-13}$ M) was achieved with excitation at 532 nm [120]. It was also shown that SMSERS signal was observed from R6G with a SER cross-section of $\sim 10^{-17}$, corresponding to an EF of $\sim 10^9$ at λ_{ex} = 633 nm [121]. Although it is clear that SMSERS intensity is maximized at the molecular resonance of R6G and that single molecules are observable with excitation frequencies off resonance, these studies were limited to fixed-frequency laser sources and were not performed on the same molecule.

To characterize the resonance Raman contributions to SMSERS intensity about the molecular resonance, surface-enhanced Raman excitation profiles (REPs) of a single R6G molecule on a Ag nanoparticle aggregate were measured using an optical parametric oscillator to
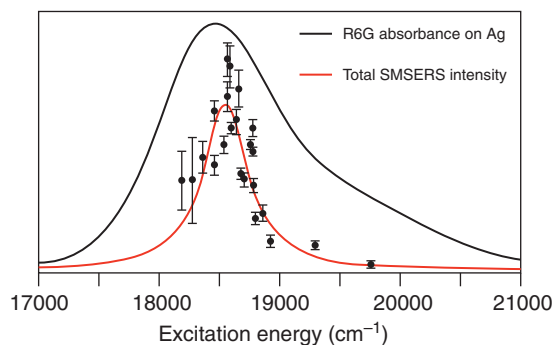
Figure 16   Surface-enhanced Raman excitation profile for a single R6G molecule fit by a Lorentzian function (red) and the ensemble-averaged surface absorbance of R6G on Ag (black).

finely tune the excitation wavelength [33]. SMSERS-active sites were identified using the isotopologue approach described earlier, and only those sites having the characteristic vibrational signature of nondeuterated R6G were used in the analysis. The single-molecule surface-enhanced REPs for three vibrational modes of R6G under dry N$_2$ were fit to single Lorentzian functions with FWHM = 365, 451, and 463 cm^{-1} for the 610, 1504, and 1647 cm^{-1} modes, respectively. As expected, a reduction in inhomogeneous broadening results in narrower linewidths for single molecules compared with those for the ensemble average. The single-molecule surface-enhanced REP representing all vibrational modes from ~ 500–1800 cm^{-1} and the ensemble-averaged surface absorbance of R6G are displayed in **Figure 16**. The single-molecule data are best fit to a Lorentzian function with $E_{max} = 18563$ cm^{-1} (538.7 nm) and FWHM = 449 cm^{-1}. In addition to being narrower than the surface absorbance data, the single-molecule data show a significant deviation from the ensemble average ($E_{max} = 18409$ cm^{-1}), which offers additional evidence for single-molecule detection. These experiments demonstrated that the structure of single-molecule surface-enhanced REPs is dominated by resonance Raman enhancement, while the magnitude is dominated by EM enhancement. In fact, DDA calculations show that changes in the EM EF as a function of excitation energy are relatively small, and the EM EF is $>10^7$ over a wide range of frequencies.

3.09.3.4   SERS Sensing Applications

Vibrational spectroscopy provides chemical specificity derived from the unique vibrational modes of different molecules, and is widely used in biological

and chemical sensing applications. However, infrared spectroscopy is greatly impeded by the strong absorbance of water, which is ubiquitous in most biological samples. Raman spectroscopy is limited by the inherent weakness of Raman scattering, resulting in insufficient sensitivity or the need for long integration times and high laser powers that can cause sample damage. SERS overcomes these limitations, and has emerged as a powerful sensing platform. The distance dependence of EM enhancement in SERS dictates that the analyte of interest must be within a few nanometers of the sensor surface. For analytes with no affinity for noble metals (i.e., Ag or Au), this can be achieved by surface modification with SAMs or thin metal oxide films, as discussed earlier.

3.09.3.4.1 In vivo *glucose sensing by SERS*

The development of *in vivo* biological sensors is particularly challenging due to the inherent complexity of the sample environment. Significant research effort has been focused on the quantitative, real-time detection of glucose, a crucial element in the management of diabetes. The feasibility of a SERS-based glucose sensor has been demonstrated using AgFON substrates functionalized with a mixed SAM consisting of decanethiol (DT) and mercaptohexanol (MH) [122]. The mixed DT/MH SAM, with dual hydrophobic/hydrophilic character, brings glucose closer to the Ag surface while excluding the interfering analytes. It also allows glucose to

departition such that a quantitative equilibrium is established, analogous to partitioning in and out of the stationary phase in high-performance liquid chromatography. A continuous *in vivo* sensor must respond rapidly and be reversible in order to accurately monitor varying glucose concentrations throughout the day, and must be stable for at least several days. To evaluate stability, SER spectra of the DT/MH-functionalized AgFON surface in bovine plasma were taken over time, and intensities were found to be stable for 10 days. To demonstrate reversibility, the DT/MH-functionalized AgFON was exposed to cycles of water and 100 mM aqueous glucose (**Figure 17(a)**). The difference spectra demonstrate partitioning of glucose into the DT/MH SAM (F, G) and complete departitioning (H, I). Analysis of real-time partitioning and departitioning data reveal a time constant of less than 1 min, indicating rapid interaction between glucose and the SAM. In addition the DT/MH-functionalized AgFON surface was shown to be stable in bovine plasma for 10 days.

An exciting advance in the development of the SERS-based glucose sensor is its successful transition from *in vitro* models to *in vivo* testing using a real animal model, the Sprague–Dawley rat. Using partial least-squares chemometric analysis, quantitative glucose detection was demonstrated *in vivo* [123]. **Figure 17(b)** shows calibration and validation data for one rat plotted on a Clarke error grid, the standard for evaluating the reliability of glucose sensors
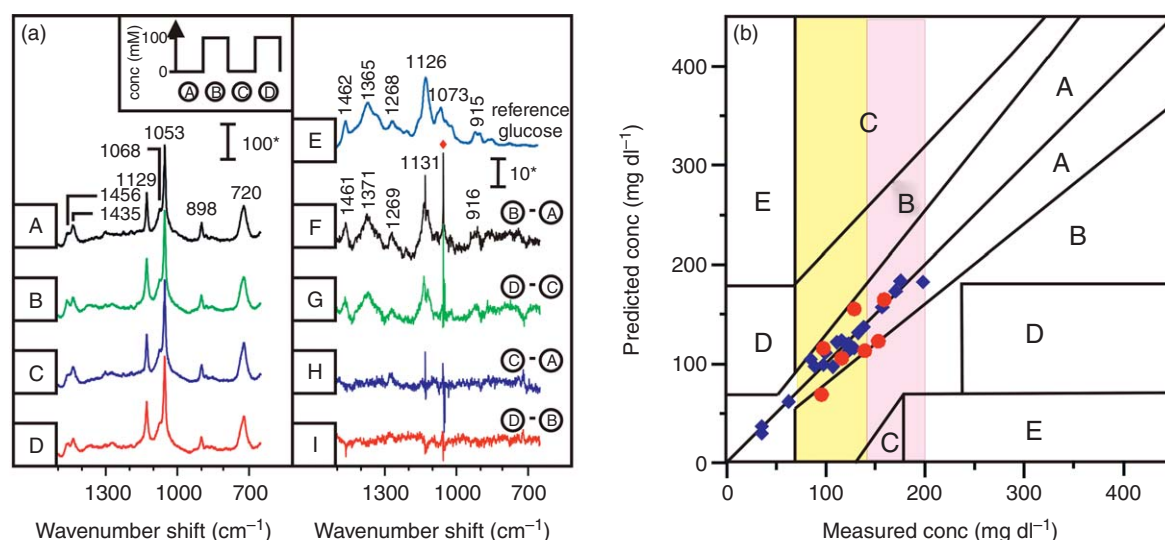
Figure 17 (a) *In vitro* and (b) *in vivo* glucose sensing using an AgFON substrate functionalized with a mixed self-assembled monolayer of decanethiol and mercaptohexanol.

in the clinically relevant concentration range. Most of the data fall within the A and B ranges, defined as areas in which the predicted values are considered to be acceptable. Data points that fall outside of these ranges lead to erroneous diagnosis or failure to identify glucose levels outside the target range. In addition to evaluating quantitative accuracy, real-time *in vivo* glucose concentrations predicted by the SERS sensor were compared with those measured simultaneously by a commercially available electro-chemical glucose sensor (Ascensia ELITE). Both sensors were able to monitor fluctuations in glucose concentration, and although the values differ, the same trends were observed.

Lastly, it was demonstrated that the DT/MH-functionalized AgFON sensor can be extended to the detection of other important biological analytes, such as lactate [124]. The potential for SERS to serve as a multi-analyte sensing platform was also shown by sequential glucose/lactate dosing with phosphate-buffered saline rinses between each step. The difference spectra demonstrate that the two analytes successfully partition and departition from the DT/MH-functionalized surface, thus demonstrating the reversibility of the sensor for multiple analytes.

### 3.09.3.4.2   Application of SERS to art conservation

The ability to detect and identify organic dyes and pigments used in historical works of art is of particular importance to the fields of art history and art conservation and restoration. For example, the identification of colorants used by an artist is useful for the authentication and dating of artwork, as well as for its long-term preservation. Thus far, high-performance liquid chromatography (HPLC) has been used to identify the largest number of colorants, but the large sample size required (∼5 mm of fiber) poses a significant challenge. An alternate method for the identification of pigments is UV–vis absorbance spectroscopy, but the broad spectra typically observed can make identification difficult, especially when a mixture is present. Raman spectroscopy has also been employed, but strong fluorescence from dye molecules is often problematic. SERS overcomes some of these limitations owing to: (1) increased sensitivity compared to NR, which reduces the amount of sample necessary for analysis; (2) molecular quenching of fluorescence near metal surfaces; and (3) identification based on unique vibrational fingerprints. In fact, the potential of SERS in

applications related to art conservation has been demonstrated in recent years by several groups [125].

The potential of SERS for problems in art conservation was first demonstrated by the successful identification of artists' dyestuffs in reference materials [126]. However, samples from real artworks are substantially more complex given the mixture of dyes present, matrix components, and the presence of contaminants. In addition, the harsh chemical extractions needed to remove the colorants from the artist's media can result in degradation of the dyes themselves. *In situ* SERS techniques, in which the surface-enhancing substrate (i.e., Ag nanoparticles) is brought to the dyed fiber have been successfully demonstrated [127, 128]. Recently, an *in situ* on-the-fiber extractionless nonhydrolysis SERS method using citrate-reduced colloids was developed and applied to authentic historical textiles [129]. As an example, this technique was performed on a single red weft fiber (0.5 mm × 2 μm) taken from a pre-Columbian Peruvian textile dated between 800 and 1350 AD (**Figure 18(a)**) [130]. Silver colloids were applied directly to the fiber and after drying it was imaged under a microscope (**Figure 18(b)**). The resulting SER spectra of the historical textile fiber and a reference wool fiber dyed with alizarin, a major dyestuff component of madder (*Rubia tinctoria L.*), are shown in **Figure 18(c)**. Despite significant aging and degradation of the fiber, the dye used to produce its red color is still easily identified as alizarin. *Galium corymbosum L.*, a Peruvian flower that contains large amounts of alizarin, was likely used to create this red color, a significant finding given the rarity of Peruvian textiles dyed with *Galium* species. Our understanding of the chronology and geographical distribution of this important colorant was therefore augmented by this work. In situations where more than one dye may be present in the sample, the coupling of thin-layer chromatography with SERS has also been shown to be a simple, effective technique capable of distinguishing dye molecules with very similar chemical structure [129].

3.09.3.4.3   SERS for chemical and biological warfare agent detection

The rapid and accurate detection of chemical and biological warfare agents is an analytical challenge of increasing significance. In addition to having high sensitivity, sensors designed for this purpose must take into account many other factors such as speed, accuracy, specificity, stability, and size. To this end, SERS-based sensors employing a portable Raman
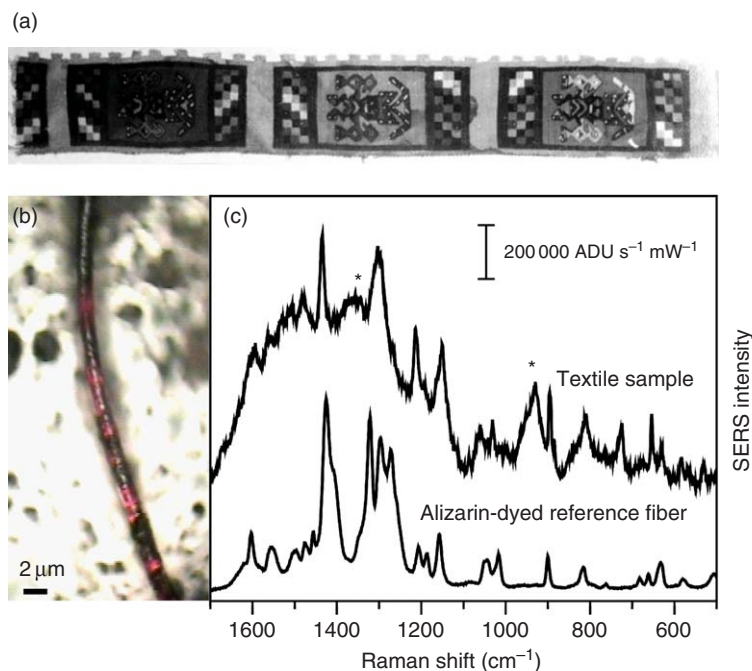
Figure 18 *In situ* on-the-fiber extractionless nonhydrolysis SERS using Ag colloidal paste. (a) Art sample (0.5 mm by 2 μm fiber) was obtained from a Peruvian textile dating to between 800 and 1350 AD, (b) coated with Ag colloidal paste, and (c) SER spectrum compared to a dyed reference fiber.

spectrometer have been developed. Initial work focused on the detection of calcium dipicolinate (CaDPA), a biomarker for anthrax [131]. CaDPA was extracted from *Bacillus subtilis* spores, a harmless simulant of *Bacillus anthracis* spores, and then drop coated on bare AgFON substrates. The SER spectrum of CaDPA displays a characteristic peak at $1020 \, cm^{-1}$. The average signal intensity of this peak from varying concentrations of CaDPA was used to construct an adsorption isotherm and determine the limit of detection (LOD). At first, peak intensity is observed to increase linearly with concentration, and then saturates at higher spore concentrations as the adsorption sites on the AgFON become fully occupied. The LOD, defined as the concentration of spores for which the SERS signal of CaDPA at $1020 \, cm^{-1}$ is equal to 3 times the background SERS signal with a 1 min data acquisition, was found to be 2600 spores, well below the anthrax infectious dose of 10^4 spores. Moreover, modification of the AgFON substrate with a thin layer of Al_2O_3 deposited by ALD improved the LOD to 1400 spores [132]. The highest signal was achieved with two ALD cycles, corresponding to a thickness of $\sim 2 \, \text{Å} \, Al_2O_3$. The optimum thickness demonstrates the trade-off between increased binding affinity of CaDPA to the

Al_2O_3 compared to silver, and decreased enhancement caused by decay of the EM field away from the surface. In addition to increasing sensitivity, the Al_2O_3 overlayer serves to protect the Ag surface from oxidation, thus improving the temporal and environmental stability of the sensor as well. SERS measurements of Al_2O_3-coated AgFONs suggest they are stable for >9 months.

The previous example highlights the ability of SERS to detect molecules introduced to the sensor from a solution containing the analyte of interest. However, detection of molecules from the gas phase is also desirable and particularly relevant for chemical warfare agents that may be released into the atmosphere. Initial experiments showed that 2-chloroethyl ethyl sulfide (CEES), a mustard gas simulant, could be detected at concentrations lower than the harmful limit, using an AgFON and a portable Raman spectrometer [133]. Recently, a detailed study has explored the potential of SERS for real-time gas phase detection of chemical warfare agents. The current leading technology for chemical sensing is ion-mobility spectrometry, which offers rapid analysis and compact instrumentation. However, there is no potential for remote sensing, and complex mixtures can be very challenging to identify. As a first
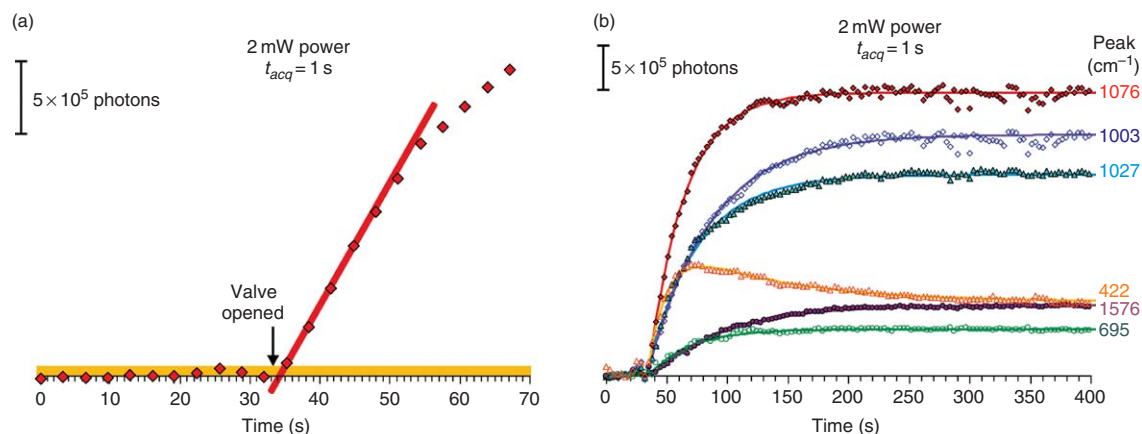
Figure 19 Real-time gas-phase sensing of benzenethiol (BT) on an AgFON. (a) SERS intensity of 8 ppm BT gas in N_2 at 358 K monitored with a portable Raman spectrometer and (b) time evolution of BT adsorption using the SERS intensity of several vibrational modes.

step toward a quantitative evaluation of SERS gas detection, the adsorption kinetics of benzenethiol on an AgFON were studied [134]. Benzenethiol was chosen as the test analyte because of its ability to form well-ordered SAMs from the gas phase. The Ag–S bond formation is irreversible under ambient conditions, and is the same mechanism responsible for irreversible binding of CEES to the AgFON previously described. For gas-phase dosing, ultrahigh purity N_2 was passed through a bubbler containing neat benzenethiol. The concentration was adjusted by dilution with N_2 downstream, and monitored by UV–vis spectroscopy before dosing to the flow cell. In order to establish how quickly molecules can be detected by SERS a detection limit time (DLt), dependent on the kinetic rate of analyte adsorption, defined as the minimum concentration that can be detected in one second of exposure for an acquisition time of 1 s and a spot size of 1.4×10^{-5} cm^2 was determined. The SERS signal detected from 8 ppm benzenthiol gas in N_2 dosed to an AgFON at 358 K was continuously monitored with a portable Raman spectrometer (**Figure 19**).

In **Figure 19(a)**, the intensity of the 1076 cm^{-1} mode of benzenethiol is plotted as a function of time. The initial rate of adsorption is linear and the detection threshold signal (three standard deviations (3σ) above the mean background signal), corresponding to 1.7×10^8 molecules or 1.8% of a monolayer, is reached in less than 1 s. **Figure 19(b)** shows the time evolution of benzenethiol adsorption using the SERS intensity of several benzenethiol modes. With the exception of the 422 cm^{-1} mode, all the peaks

grow in according to first-order Langmuir kinetics. The 422 cm^{-1} mode displays a double-exponential behavior that is thought to result from the strong dependence of this particular mode's EM enhancement on surface orientation. The DLt was calculated to be 6 ppm-s for benzenethiol gas adsorption on an AgFON at 358 K with an acquisition time of 1 s. The DLt is fundamentally limited by the low sticking probability of benzenethiol, which was found to be 1.5×10^{-5}. The sticking probability increases with increasing temperature and the slope of the Arrhenius plot yields an activation barrier of ~13 kJ mol^{-1}. Therefore, the sensitivity of this sensor may be improved by increasing the sticking probability of the analyte, highlighting the importance of surface functionalization to optimize analyte affinity. These quantitative experiments present significant progress toward the goal of real-time gas detection of chemical warfare agents based on SERS.

3.09.4 Future Directions

3.09.4.1 New Plasmonic Materials for SERS

Despite the extraordinary surface sensitivity of SERS and the wealth of chemical information it provides, it is largely limited to studies on noble-metal nanostructured surfaces. Although Au and Ag are the mainstays of current LSPR and SERS technology, they are expensive materials and do not support plasmons in the UV region, representing an obstacle to next-generation biological investigations. Yet, in theory, any material that exhibits a negative real and

small positive imaginary dielectric function may support surface plasmons. A number of other metals (i.e., Li, Na, Al, In, Ga, and Cu) meet this criterion but have not been widely implemented in plasmonic applications, in part due to problems associated with instability or oxidation. Surface oxidation is especially problematic as it may significantly alter the optical properties of the metal nanostructure. In some cases, it is possible to overcome this problem by removing the oxide layer with an appropriate etchant. For example, Cu is oxidized upon exposure to ambient atmosphere to form a surface layer of Cu oxides (Cu_2O and CuO) [135]. However, glacial acetic acid was found to be effective for removing the layer of Cu oxides on Cu nanoparticles without modifying the Cu metal surface [136]. Whereas untreated Cu nanoparticles fabricated by NSL exhibit broad and weak LSPR spectra, removal of the oxidized layer results in comparatively narrower and more intense extinction spectra. Electrodynamics calculations on a Cu nanoparticle coated by a Cu oxide shell of varying thickness confirmed the oxidation-induced changes to the LSPR. According to AFM and SEM images of the Cu nanoparticles, the oxide layer is of subnanometer thickness and was formed just after exposure to ambient laboratory conditions. Importantly, acid treatment did not significantly alter the shape or height of the Cu nanoparticles. Using NSL fabrication, the LSPR of Cu nanoparticles was tuned throughout the visible region, and exhibited comparable peak intensities and linewidths to Ag and Au arrays when the LSPR λ_{max} is > ∼650 nm. The results of these investigations suggest that Cu, a relatively inexpensive metal, may be useful to replace Ag and Au for certain LSPR and SERS applications.

The plasmon resonance condition for Ag and Au nanoparticles is met in the visible and NIR regions of the EM spectrum. However, the development of nanostructured materials capable of supporting surface plasmons in the UV region is interesting for the potential application of UV SERS. Ultraviolet excitation would be advantageous for interrogating samples with electronic resonances in the UV, as is the case with many biological molecules, in order to benefit from combined resonance Raman and EM enhancement effects. From the dielectric functions of Ag and Al (**Figure 2**), it is evident that Ag cannot support surface plasmons below ∼350 nm, where the real part of its dielectric function is positive, whereas Al should support plasmons from 200 to ∼800 nm. Indeed, several recent studies of the plasmonic properties of Al have shown that Al nanoparticle arrays
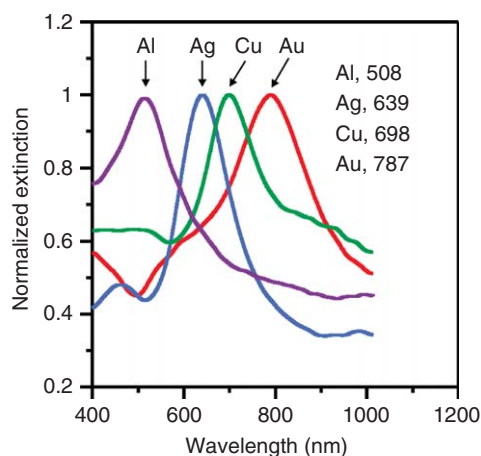
Figure 20   LSPR spectra of nanoparticle arrays with identical geometries but varying metal (Al, Ag, Cu, or Au).

support localized surface plasmons throughout the UV–vis NIR spectrum [24, 137, 138]. Aluminum, however, is extremely reactive to oxygen and upon exposure to ambient conditions immediately forms a thin (∼2–3 nm) Al_2O_3 layer that prevents further attack by oxygen. Interestingly, for Al nanoparticles fabricated by NSL, SEM images reveal a sharp contrast between the tips and the core of the triangular nanoparticles, suggesting concentrated oxide formation at the nanoparticle tips [24]. The native oxide shell results in a red-shifted LSPR, owing to the dielectric sensitivity of the LSPR, but does not exhibit the dampening effect of Cu oxides. However, both experimental and theoretical data show that when the LSPR of the nanoparticles is close to the Al interband transition (∼800 nm), the LSPR is significantly broadened. A comparison of the normalized LSPR extinction spectra for Al, Ag, Cu, and Au nanoparticles of the same geometry, all fabricated by NSL, is shown in **Figure 20**. In general, Al nanoparticles exhibited a bluer, broader, and less intense LSPR compared to the other metals in the visible region. In the UV region, however, Al is a superior plasmonic material, and the potential utility of NSL Al triangular arrays as a substrate for UV SERS is currently under investigation. Undoubtedly, future advances in LSPR and SERS applications will rely on broadening the plasmonic periodic table to new materials as well as novel nanostructures.

3.09.4.2   Novel Nanostructures

Although more than 20 years have passed since the discovery of SERS, some of the fundamental

questions have remained unanswered. For example, what nanoparticle structure or array provides the highest EM enhancement? This question is significant since the development of next-generation LSPR- and SERS-based sensors requires that the most enhancing nanoparticles and nanoparticle arrays are developed. Therefore, an understanding of the fundamental relationships among the SER scattering intensity, LSPR, and nanoparticle structure must be established. Toward this end, recent interest has focused on correlated investigations of structure (i.e., with AFM or TEM imaging) and LSPR for individual nanoparticles as well as the corresponding SER spectra for adsorbed analytes, which provide the ability to measure the fundamental relationships between the structural and optical properties at the single-particle level, unobscured by ensemble averaging.

Recent advances in nanofabrication techniques have enabled the development of new nanostructures for LSPR and SER spectroscopy. For example, novel chemical synthetic methods have provided a plethora of novel nanoparticle shapes, sizes, and functionalities including Ag nanocubes [38, 139], Ag and Au nanoprisms [36], and stabilized spherical aggregates [140]. In order to determine the optimal nanostructures for LSPR and SERS sensing as well as how such nanoparticles can be incorporated in next-generation devices, the detailed relationship between the optical response and structural properties of single nanoparticles is under investigation. Cube-shaped nanoparticles fabricated using polyol synthesis [38] exhibit two LSPR maxima owing to the asymmetry induced by surface immobilization on glass [141]. Both LSPR peaks are sensitive to changes in dielectric environment, but the blue-shifted resonance has superior LSPR sensing capabilities due to its sharpness [142]. In addition, correlated LSPR and HRTEM measurements of individual Ag nanocubes revealed the dependence of the LSPR on nanocube size and shape. Corresponding electrodynamics calculations demonstrated the strong sensitivity between the nanocube optical response and the face-to-face width, corner and side rounding, and substrate of each nanocube. In a related study, correlated high-resolution SEM and polarization-dependent SERS measurements were performed on individual Ag nanocubes [143]. Although the Ag nanocube samples appeared monodisperse, various SER scattering intensities were observed from individual nanocubes as a result of nanoparticle orientation relative to the exciting laser field. Ensemble-averaged SERS experiments on the nanocubes reveal that the overall average EF is $\sim 10^5$, although detailed studies at the single-nanoparticle level are needed to elucidate the underlying details of the EM enhancement [144].

The most desirable single-particle experiment is to measure the structure, LSPR, and SER scattering intensity of the same nanoparticle. At present, SMSERS experiments have provided the best example of this correlated study. In particular, SMSERS investigations (Section 3.09.3.3.3) of individual R6G molecules on aggregated Ag colloids demonstrated that hot spots located between nanoparticles are responsible for the enhanced fields that enable single-molecule detection [32, 145]. However, the Ag colloids used in the majority of SMSERS experiments are randomly aggregated using electrolyte solutions and do not provide controlled, homogeneous structures. Toward this end, novel nanostructures composed of a stabilizing shell around a well-defined metallic core have been developed. For example, silica-encapsulated SERS nanotags containing Au cores, a layer of a SERS 'reporter' molecule, and silica shell have demonstrated structural uniformity, optical robustness, and the capability to use bio-relevant reporter molecules [140]. Moreover, these SERS nanotags provide an excellent system in which to study the structure–property relationships for well-defined and easily controlled nanoparticle geometries (e.g., monomers, dimers) [146]. Ultimately, correlated studies performed at the single-nanoparticle level on novel nanostructures such as nanocubes and silica-coated nanospheres hold the promise for the development of robust and high-enhancing SERS substrates and these studies are underway.

3.09.4.3 Tip-Enhanced Raman Spectroscopy

In addition to exploring new plasmonic materials and nanostructures, other successful approaches have been used to broaden the applicability and generality of SERS. One significant challenge to achieving a truly general SERS substrate is that surface functionalization is often required to facilitate the binding of specific analytes to specific surfaces. For example, thin catalytically active transition metal overlayers were electrodeposited on roughened Au in order to study catalytic reactions with SERS [147]. This chapter highlighted other types of overlayers such as SAMs and thin metal oxide films that are used to functionalize the surface of a SERS substrate. However, perhaps the most promising technique for
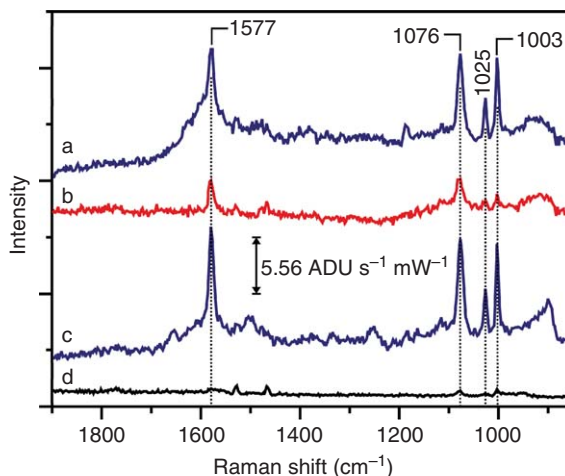
Figure 21 Tip-enhanced Raman spectra for BT adsorbed to an 8-nm Au island film. (a) AFM tip engaged, (b) tip withdrawn by 100 μm, (c) tip re-engaged, and (d) sample removed with laser focused on the tip.

achieving complete substrate generality is TERS. In TERS, enhancement arises from a noble metal scanning probe microscopy (SPM) tip rather than from the substrate. When the tip is irradiated with visible light, there is a corresponding excitation of its LSPR. The resulting EM enhancement near the tip apex is used to increase the Raman scattering from molecules in the vicinity of the tip, even without direct adsorption. The Raman scattering intensities of molecules located in the near-field region of Ag or Au SPM tips are enhanced by three to six orders of magnitude [148]. Moreover, the use of an SPM tip provides nanometer-scale resolution, a significant improvement to the diffraction-limited spatial resolution of SERS, which is approximately $\lambda_{ex}/2$ or ~250 nm for visible excitation.

Figure 21 presents representative TER spectra for benzenethiol adsorbed to an 8-nm Au island film (AuIF) that is weakly SERS active at $\lambda_{ex} = 532$ nm. In spectrum 'a', the AFM tip that is coated with 40-nm Ag is engaged and makes contact with the sample yielding a high signal-to-noise ratio TER spectrum. In 'b', the tip is withdrawn from the sample by 100 μm, while the laser spot remains focused on the sample. When the AFM tip is re-engaged in contact mode, the same high signal-to-noise TER spectrum is observed (c). After several engage–disengage cycles, the sample was removed and the spectrum (d) was taken with the laser focused on the AFM tip. These results demonstrate that benzenethiol molecules were not transferred from the AuIF to the tip, and thus the observed TERS signal originated from the molecules adsorbed on the Au

surface. By taking the difference in surface area between the laser spot ($\sim 1\,\mu m^2$) and the contact area of the AFM tip ($\sim 300\,nm^2$) into account, the average EF is estimated to be $>10^4$, demonstrating the sensitivity resulting from tip enhancement.

TERS combines the high sensitivity and rich chemical information content of SERS with the excellent spatial resolution provided by scanning probe microscopy. In addition, ultrahigh vacuum (UHV) TERS provides integration of laser excitation and scanning tunneling microscopy (STM) capabilities and permits atomic resolution and structural elucidation of adsorbate molecules on clean, single-crystal or nanostructured surfaces in a controlled environment. In a recent UHV-TERS study, TER imaging of a single brilliant cresyl blue molecule with a spatial resolution of 15 nm was demonstrated [6]. Although TERS is still in the early stages of development, the results of these experiments demonstrate that TERS will be a powerful tool for probing chemical problems in catalysis, surface science, tribology, biological science, and nanomaterials.

3.09.5   Conclusion

In this chapter we aimed to present an overall description of nanostructures, LSPR, and SERS through fundamental expressions as well as experimental investigations. The research highlighted here demonstrates a promising future for SERS and significant implications for the field of nanoscience and technology.

Acknowledgments

References

1. Jeanmaire DL and Van Duyne RP (1977) Surface Raman spectroelectrochemistry. Part I. Heterocyclic, aromatic, and aliphatic amines adsorbed on the anodized silver electrode. *Journal of Electroanalytical Chemistry and Interfacial Electrochemistry* 84: 1–20.
2. Albrecht MG and Creighton JA (1977) Anomalously intense Raman spectra of pyridine at a silver electrode. *Journal of the American Chemical Society* 99: 5215–5217.
3. Kneipp K, Wang Y, Kneipp H, *et al.* (1997) Single molecule detection using surface-enhanced Raman scattering (SERS). *Physical Review Letters* 78: 1667–1670.
4. Nie SM and Emory SR (1997) Probing single molecules and single nanoparticles by surface-enhanced Raman scattering. *Science* 275: 1102–1106.
5. Neacsu CC, Dreyer J, Behr N, and Raschke MB (2006) Scanning-probe Raman spectroscopy with single-molecule sensitivity. *Physical Review B* 73: 4.
6. Steidtner J and Pettinger B (2008) Tip-enhanced Raman spectroscopy and microscopy on single dye molecules with 15 nm resolution. *Physical Review Letters* 100: 236101/236101–236101/236104.
7. Brill RH (1965) The chemistry of the Lycurgus cup. In: *Proceedings of the 7th International Congress on Glass*, *comptes rendus 2*, pp. 1–13, Bruxelles.
8. Barber DJ and Freestone IC (1990) An investigation of the origin of the colour of the Lycurgus cup by analytical transmission electron microscopy. *Archaeometry* 32: 33–45.
9. Faraday M (1857) The Bakerian lecture: Experimental relations of gold (and other metals) to light. *Philosophical Transactions of the Royal Society of London* 147: 145–181.
10. Willets KA and Van Duyne RP (2007) Localized surface plasmon resonance spectroscopy and sensing. *Annual Review of Physical Chemistry* 58: 267–297.
11. Haes AJ and Van Duyne RP (2004) A unified view of propagating and localized surface plasmon resonance biosensors. *Analytical and Bioanalytical Chemistry* 379: 920–930.
12. Yonzon CR, Jeoung E, Zou S, *et al.* (2004) A comparative analysis of localized and propagating surface plasmon resonance sensors: The binding of concanavalin A to a monosaccharide functionalized self-assembled monolayer. *Journal of the American Chemical Society* 126: 12669–12676.
13. Hall WP, Anker JN, Lin Y, *et al.* (2008) A calcium-modulated plasmonic switch. *Journal of the American Chemical Society* 130: 5836–5837.
14. Mie G (1908) Contributions to the optics of turbid media, especially colloidal metal solutions. *Annalen der Physik (Weinheim, Germany)* 25: 377–445.
15. Kelly KL, Coronado E, Zhao LL, and Schatz GC (2003) The optical properties of metal nanoparticles: The influence of size, shape, and dielectric environment. *Journal of Physical Chemistry B* 107: 668–677.
16. Gans R (1912) The form of ultramicroscopic gold particles. *Annalen der Physik (Weinheim, Germany)* 37: 881–900.
17. Gans R (1915) Form of ultramicroscopic particles of silver. *Annalen der Physik (Berlin, Germany)* 47: 270–284.
18. Kelly KL, Jensen TR, Lazarides AA, and Schatz GC (2002) Modeling metal nanoparticles optical properties. *Metal Nanoparticles: Synthesis, Characterization, and Applications*. pp 88–118. New York: Marcel Dekker, Inc.
19. Feynman RP, Leighton RB, and Sands M (1964) *The Feynman Lectures on Physics*. Reading, MA: Addison-Wesley.
20. Doyle WT (1989) Optical properties of a suspension of metal spheres. *Physical Review B* 39: 9852.
21. Sherry LJ, Jin R, Mirkin CA, Schatz GC, and Van Duyne RP (2006) Localized surface plasmon resonance spectroscopy of single silver triangular nanoprisms. *Nano Letters* 6: 2060–2065.
22. Hecht E (1998) *Optics*. New York: Addison-Wesley.
23. Bohren CF and Huffman DR (1983) *Absorption and Scattering of Light by Small Particles*. New York: Wiley.
24. Chan GH, Zhao J, Schatz GC, and Van Duyne RP (2008) Localized surface plasmon resonance spectroscopy of triangular aluminum nanoparticles. *Journal of Physical Chemistry C* 112: 13958–13963.
25. Stiles PL, Dieringer JA, Shah NC, and Van Duyne RP (2008) Surface-enhanced Raman spectroscopy. *Annual Review of Analytical Chemistry* 1: 601–626.
26. Jung LS, Campbell CT, Chinowsky TM, Mar MN, and Yee SS (1998) Quantitative interpretation of the response of surface plasmon resonance sensors to adsorbed films. *Langmuir* 14: 5636–5648.
27. Schatz GC (2001) Electrodynamics of nonspherical noble metal nanoparticles and nanoparticle aggregates. *Journal of Molecular Structure (Theochem)* 573: 73–80.
28. Purcell EM and Pennypacker CR (1973) Scattering and absorption of light by nonspherical dielectric grains. *Astrophysical Journal* 186: 705–714.
29. McFarland AD and Van Duyne RP (2003) Single silver nanoparticles as real-time optical sensors with zeptomole sensitivity. *Nano Letters* 3: 1057–1062.
30. Billaud P, Huntzinger JR, Cottancin E, *et al.* (2007) Optical extinction spectroscopy of single silver nanoparticles. *European Physical Journal D: Atomic, Molecular, Optical and Plasma Physics* 43: 271–274.
31. Lee PC and Meisel D (1982) Adsorption and surface-enhanced Raman of dyes on silver and gold sols. *Journal of Physical Chemistry* 86: 3391–3395.
32. Dieringer JA, Lettan RB, II, Scheidt KA, and Van Duyne RP (2007) A frequency domain existence proof of single-molecule surface-enhanced Raman spectroscopy. *Journal of the American Chemical Society* 129: 16249–16256.
33. Dieringer JA, Wustholz KL, Masiello DJ, *et al.* (2009) Surface-enhanced Raman excitation spectroscopy of a single Rhodamine 6G molecule. *Journal of the American Chemical Society* 131: 849–854.
34. Camden JP, Dieringer JA, Wang Y, *et al.* (2008) Probing the structure of single-molecule surface-enhanced Raman

scattering hot spots. *Journal of the American Chemical Society* 130: 12616–12617.

35. Oldenburg SJ, Oldenburg SJ, Averitt RD, Westcott SL, and Halas NJ (1998) Nanoengineering of optical resonances. *Chemical Physics Letters* 288: 243–247.

36. Jin RC, Cao YW, Mirkin CA, *et al.* (2001) Photo induced conversion of silver nanospheres to nanoprisms. *Science* 294: 1901–1903.

37. Sun Y and Xia Y (2002) Shape-controlled synthesis of gold and silver nanoparticles. *Science (New York)* 298: 2176–2179.

38. Siekkinen AR, McLellan JM, Chen JY, and Xia YN (2006) Rapid synthesis of small silver nanocubes by mediating polyol reduction with a trace amount of sodium sulfide or sodium hydrosulfide. *Chemical Physics Letters* 432: 491–496.

39. Wiley BJ, Xiong Y, Li Z-Y, Yin Y, and Xia Y (2006) Right bipyramids of silver: A new shape derived from single twinned seeds. *Nano Letters* 6: 765–768.

40. Nehl CL, Liao H, and Hafner JH (2006) Optical properties of star-shaped gold nanoparticles. *Nano Letters* 6: 683–688.

41. Amendola V and Meneghetti M (2009) Laser ablation synthesis in solution and size manipulation of noble metal nanoparticles. *Physical Chemistry – Chemical Physics* 11: 3805–3821.

42. Fojtik A, Giersig M, and Henglein A (1993) Formation of nanometer-size silicon particles in a laser induced plasma in SiH_4. *Berichte der Bunsen-Gesellschaft* 97: 1493–1496.

43. Van Duyne RP, Hulteen JC, and Treichel DA (1993) Atomic force microscopy and surface-enhanced Raman spectroscopy. I. Silver island films and silver film over polymer nanosphere surfaces supported on glass. *Journal of Chemical Physics* 99: 2101–2115.

44. Fleischmann M, Hendra PJ, and McQuillan AJ (1974) Raman spectra of pyridine adsorbed at a silver electrode. *Chemical Physics Letters* 26: 163–166.

45. Haynes CL, McFarland AD, Zhao L, *et al.* (2003) Nanoparticle optics: The importance of radiative dipole coupling in two-dimensional nanoparticle arrays. *Journal of Physical Chemistry B* 107: 7337–7342.

46. Hicks EM, Gunnarrsson L, Rindevicius T, *et al.* (2005) Investigating narrow plasmons in nanoparticle arrays fabricated using electron beam lithography. *Materials Research Society Symposium Proceedings* 872: 317–322.

47. McLellan E, Gunnarsson L, Rindzevicius T, *et al*. (2007) Plasmonic and diffractive coupling in two-dimensional arrays of nanoparticles produced by electron beam lithography. In: *Materials Research Society Symposium Proceedings*, 951E, 0951-E0909-0920.

48. Sung J, Hicks EM, Van Duyne RP, and Spears KG (2007) Nanoparticle spectroscopy: Dipole coupling in two-dimensional arrays of L-shaped silver nanoparticles. *Journal of Physical Chemistry C* 111: 10368–10376.

49. Sung J, Hicks EM, Van Duyne RP, and Spears KG (2008) Nanoparticle spectroscopy: Plasmon coupling in finite-sized two-dimensional arrays of cylindrical silver nanoparticles. *Journal of Physical Chemistry C* 112: 4091–4096.

50. Henzie J, Lee J, Lee MH, Hasan W, and Odom TW (2009) Nanofabrication of plasmonic structures. *Annual Review of Physical Chemistry* 60: 147–165.

51. Sundaramurthy A, Schuck PJ, Conley NR, *et al.* (2006) Toward nanometer-scale optical photolithography: Utilizing the near-field of bowtie optical nanoantennas. *Nano Letters* 6: 355–360.

52. Hulteen JC and Van Duyne RP (1995) Nanosphere lithography: A materials general fabrication process for periodic particle array surfaces. *Journal of Vacuum Science and Technology A: Vacuum, Surfaces, and Films* 13: 1553–1558.

53. Haynes CL and Van Duyne RP (2001) Nanosphere lithography: A versatile nanofabrication tool for studies of size-dependent nanoparticle optics. *Journal of Physical Chemistry B* 105: 5599–5611.

54. Haynes CL, McFarland AD, Smith MT, Hulteen JC, and Van Duyne RP (2002) Angle-resolved nanosphere lithography: Manipulation of nanoparticle size, shape, and interparticle spacing. *Journal of Physical Chemistry B* 106: 1898–1902.

55. Hicks EM, Lyandres O, Hall WP, *et al.* (2007) Plasmonic properties of anchored nanoparticles fabricated by reactive ion etching and nanosphere lithography. *Journal of Physical Chemistry C* 111: 4116–4124.

56. Zhao J, Haes AJ, Zhang X, *et al.* (2006) Alkanethiol mediated release of surface bound nanoparticles fabricated by nanosphere lithography. In: *Materials Research Society Symposium Proceedings*, 900E, 0900-O0913-0908.

57. Haes AJ, Zhao J, Zou S, *et al.* (2005) Solution-phase, triangular Ag nanotriangles fabricated by nanosphere lithography. *Journal of Physical Chemistry B* 109: 11158–11162.

58. Zhang X, Hicks EM, Zhao J, Schatz GC, and Van Duyne RP (2005) Electrochemical tuning of silver nanoparticles fabricated by nanosphere lithography. *Nano Letters* 5: 1503–1507.

59. Jensen TR, Duval ML, Kelly KL, *et al.* (1999) Nanosphere lithography: Effect of the external dielectric medium on the surface plasmon resonance spectrum of a periodic array of silver nanoparticles. *Journal of Physical Chemistry B* 103: 9846–9853.

60. Malinsky MD, Kelly KL, Schatz GC, and Van Duyne RP (2001) Chain length dependence and sensing capabilities of the localized surface plasmon resonance of silver nanoparticles chemically modified with alkanethiol self-assembled monolayers. *Journal of the American Chemical Society* 123: 1471–1482.

61. Raschke G, Kowarik S, Franzl T, *et al.* (2003) Biomolecular recognition based on single gold nanoparticle light scattering. *Nano Letters* 3: 935–938.

62. Mock JJ, Barbic M, Smith DR, Schultz DA, and Schultz S (2002) Shape effects in plasmon resonance of individual colloidal silver nanoparticles. *Journal of Chemical Physics* 116: 6755–6759.

63. Haes AJ and Van Duyne RP (2002) A nanoscale optical biosensor: Sensitivity and selectivity of an approach based on the localized surface plasmon resonance spectroscopy of triangular silver nanoparticles. *Journal of the American Chemical Society* 124: 10596–10604.

64. Riboh JC, Haes AJ, McFarland AD, Yonzon CR, and Van Duyne RP (2003) A nanoscale optical biosensor: Real-time immunoassay in physiological buffer enabled by improved nanoparticle adhesion. *Journal of Physical Chemistry B* 107: 1772–1780.

65. Haes AJ, Hall WP, Chang L, Klein WL, and Van Duyne RP (2004) A localized surface plasmon resonance biosensor: First steps toward an assay for Alzheimer's disease. *Nano Letters* 4: 1029–1034.

66. Haes AJ, Chang L, Klein WL, and Van Duyne RP (2005) Detection of a biomarker for Alzheimer's disease from synthetic and clinical samples using a nanoscale optical biosensor. *Journal of the American Chemical Society* 127: 2264–2271.

67. El-Sayed IH, Huang X, and El-Sayed MA (2005) Surface plasmon resonance scattering and absorption of anti-EGFR antibody conjugated gold nanoparticles in cancer diagnostics: Applications in oral cancer. *Nano Letters* 5: 829–834.

68. Anker JN, Hall WP, Lyandres O, *et al.* (2008) Biosensing with plasmonic nanosensors. *Nature Materials* 7: 442–453.
69. Yonzon CR, Stuart DA, Zhang X, *et al.* (2005) Towards advanced chemical and biological nanosensors – an overview. *Talanta* 67: 438–448.
70. Stuart DA, Haes AJ, Yonzon CR, Hicks EM, and Van Duyne RP (2005) Biological applications of localized surface plasmonic phenomena. *IEE Proceedings: Nanobiotechnology* 152: 13–32.
71. Whitney AV, Elam JW, Zou S, *et al.* (2005) Localized surface plasmon resonance nanosensor: A high-resolution distance-dependence study using atomic layer deposition. *Journal of Physical Chemistry B* 109: 20522–20528.
72. Haes AJ, Zou S, Schatz GC, and Van Duyne RP (2004) A nanoscale optical biosensor: The long range distance dependence of the localized surface plasmon resonance of noble metal nanoparticles. *Journal of Physical Chemistry B* 108: 109–116.
73. Haes AJ, Zou S, Schatz GC, and Van Duyne RP (2004) Nanoscale optical biosensor: Short range distance dependence of the localized surface plasmon resonance of noble metal nanoparticles. *Journal of Physical Chemistry B* 108: 6961–6968.
74. Reinhard BM, Siu M, Agarwal H, Alivisatos AP, and Liphardt J (2005) Calibration of dynamic molecular rulers based on plasmon coupling between gold nanoparticles. *Nano Letters* 5: 2246–2252.
75. Soennichsen C, Reinhard BM, Liphardt J, and Alivisatos AP (2005) A molecular ruler based on plasmon coupling of single gold and silver nanoparticles. *Nature Biotechnology* 23: 741–745.
76. Storhoff JJ, Lazarides AA, Mucic RC, *et al.* (2000) What controls the optical properties of DNA-linked gold nanoparticle assemblies? *Journal of the American Chemical Society* 122: 4640–4650.
77. Ritala M and Leskela M (2002) Atomic layer deposition. In: Naiwa HS (ed.) *Handbook of Thin Film Materials*, vol. 1, pp. 103–159. San Diego, CA: Academic Press.
78. Puurunen RL (2005) Surface chemistry of atomic layer deposition: A case study for the trimethylaluminum/water process. *Journal of Applied Physics* 97: 52.
79. Ott AW, Klaus JW, Johnson JM, and George SM (1997) Al3O3 thin film growth on Si(100) using binary reaction sequence chemistry. *Thin Solid Films* 292: 135–144.
80. Sung J, Kosuda KM, Zhao J, *et al.* (2008) Stability of silver nanoparticles fabricated by nanosphere lithography and atomic layer deposition to femtosecond laser excitation. *Journal of Physical Chemistry C* 112: 5707–5714.
81. Whitney AV, Elam JW, Stair PC, and Van Duyne RP (2007) Toward a thermally robust operando surface-enhanced Raman spectroscopy substrate. *Journal of Physical Chemistry C* 111: 16827–16832.
82. Haes AJ, Haynes CL, McFarland AD, *et al.* (2005) Plasmonic materials for surface-enhanced sensing and spectroscopy. *MRS Bulletin* 30: 368–375.
83. Roark SE, Semin DJ, Lo A, Skodje RT, and Rowlen KL (1995) Solvent-induced morphology changes in thin silver films. *Analytica Chimica Acta* 307: 341–353.
84. Raman CV and Krishnan KS (1928) A new type of secondary radiation. *Nature* 121: 501–502.
85. McCreery RL (2000) *Raman Spectroscopy for Chemical Analysis*. New York: Wiley.
86. Campion A and Kambhampati P (1998) Surface-enhanced Raman scattering. *Chemical Society Reviews* 27: 241–250.
87. Otto A, Mrozek I, Grabhorn H, and Akemann W (1992) Surface-enhanced Raman-scattering. *Journal of Physics: Condensed Matter* 4: 1143–1212.
88. Burstein E, Chen YJ, Chen CY, Lundquist S, and Tosatti E (1979) ''Giant'' Raman scattering by adsorbed molecules on metal surfaces. *Solid State Communications* 29: 567–570.
89. Gersten JI, Birke RL, and Lombardi JR (1979) Theory of enhance I light scattering from molecules adsorbed at the metal–solution interface. *Physical Review Letters* 43: 147.
90. Lombardi JR, Birke RL, Lu T, and Xu J (1986) Charge-transfer theory of surface enhanced Raman spectroscopy: Herzberg–Teller contributions. *Journal of Chemical Physics* 84: 4174.
91. Billmann J and Otto A (1982) Electronic surface state contribution to surface enhanced Raman scattering. *Solid State Communications* 44: 105–107.
92. Furtak TE and Macomber SH (1983) Voltage-induced shifting of charge-transfer excitations and their role in surface-enhanced Raman scattering. *Chemical Physics Letters* 95: 328–332.
93. Lombardi JR, Birke RL, Sanchez LA, Bernard I, and Sun SC (1984) The effect of molecular structure on voltage induced shifts of charge transfer excitation in surface enhanced Raman scattering. *Chemical Physics Letters* 104: 240–247.
94. Moskovits M (1985) Surface-enhanced spectroscopy. *Reviews of Modern Physics* 57: 783.
95. Kerker M, Wang D-S, and Chew H (1980) Surface enhanced Raman scattering (SERS) by molecules adsorbed at spherical particles: Errata. *Applied Optics* 19: 4159–4174.
96. Wang DS and Kerker M (1981) Enhanced Raman-scattering by molecules adsorbed at the surface of colloidal spheroids. *Physical Review B* 24: 1777–1790.
97. McFarland AD, Young MA, Dieringer JA, and Van Duyne RP (2005) Wavelength-scanned surface-enhanced Raman excitation spectroscopy. *Journal of Physical Chemistry B* 109: 11279–11285.
98. Kennedy BJ, Spaeth S, Dickey M, and Carron KT (1999) Determination of the distance dependence and experimental effects for modified SERS substrates based on self-assembled monolayers formed using alkanethiols. *Journal of Physical Chemistry B* 103: 3640–3646.
99. Dieringer JA, McFarland AD, Shah NC, *et al.* (2006) Surface enhanced Raman spectroscopy: New materials, concepts, characterization tools, and applications. *Faraday Discussions* 132: 9–26.
100. Blatchford CG, Campbell JR, and Creighton JA (1982) Plasma resonance enhanced Raman-scattering by adsorbates on gold colloids – the effects of aggregation. *Surface Science* 120: 435–455.
101. Felidj N, Aubard J, Levi G, *et al.* (2003) Optimized surface-enhanced Raman scattering on gold nanoparticle arrays. *Applied Physics Letters* 82: 3095–3097.
102. Vlckova B, Gu XJ, and Moskovits M (1997) SERS excitation profiles of phthalazine adsorbed on single colloidal silver aggregates as a function of cluster size. *Journal of Physical Chemistry B* 101: 1588–1593.
103. Haes AJ, Zou SL, Zhao J, Schatz GC, and Van Duyne RP (2006) Localized surface plasmon resonance spectroscopy near molecular resonances. *Journal of the American Chemical Society* 128: 10905–10914.
104. Wiederrecht GP, Wurtz GA, and Hranisavljevic J (2004) Coherent coupling of molecular excitons to electronic polarizations of noble metal nanoparticles. *Nano Letters* 4: 2121–2125.
105. Wurtz GA, Evans PR, Hendren W, *et al.* (2007) Molecular plasmonics with tunable exciton–plasmon coupling strength in J-aggregate hybridized Au nanorod assemblies. *Nano Letters* 7: 1297–1303.

106. Zhao J, Jensen L, Sung JH, *et al.* (2007) Interaction of plasmon and molecular resonances for Rhodamine 6G adsorbed on silver nanoparticles. *Journal of the American Chemical Society* 129: 7647–7656.

107. Zhao J, Dieringer JA, Zhang X, Schatz GC, and Van Duyne RP (2008) Wavelength-scanned surface-enhanced resonance Raman excitation spectroscopy. *Journal of Physical Chemistry C* 112: 19302–19310.

108. Zhao J, Das A, Zhang XY, *et al.* (2006) Resonance surface plasmon spectroscopy: Low molecular weight substrate binding to cytochrome P450. *Journal of the American Chemical Society* 128: 11004–11005.

109. Andersen PC, Jacobson ML, and Rowlen KL (2004) Flashy silver nanoparticles. *Journal of Physical Chemistry B* 108: 2148–2153.

110. Domke KF, Zhang D, and Pettinger B (2007) Enhanced Raman spectroscopy: Single molecules or carbon? *Journal of Physical Chemistry C* 111: 8611–8616.

111. Etchegoin PG, Meyer M, and Le Ru EC (2007) Statistics of single molecule SERS signals: Is there a Poisson distribution of intensities? *Physical Chemistry Chemical Physics* 9: 3006–3010.

112. Doering WE and Nie SM (2002) Single-molecule and single-nanoparticle SERS: Examining the roles of surface active sites and chemical enhancement. *Journal of Physical Chemistry B* 106: 311–317.

113. Etchegoin PG, Meyer M, Blackie E, and Le Ru EC (2007) Statistics of single-molecule surface enhanced Raman scattering signals: Fluctuation analysis with multiple analyte techniques. *Analytical Chemistry* 79: 8411–8415.

114. Le Ru EC, Meyer M, and Etchegoin PG (2006) Proof of single-mokeule sensitivity in surface enhanced Raman scattering (SERS) by means of a two-analyte technique. *Journal of Physical Chemistry B* 110: 1944–1948.

115. Noda I and Ozaki Y (2004) *Two-Dimensional Correlation Spectroscopy: Applications in Vibrational and Optical Spectroscopy.* Chichester: Wiley.

116. Moore AA, Jacobson ML, Belabas N, Rowlen KL, and Jonas DM (2005) 2D correlation analysis of the continuum in single molecule surface enhanced Raman spectroscopy. *Journal of the American Chemical Society* 127: 7292–7293.

117. Jiang J, Bosnick K, Maillard M, and Brus L (2003) Single molecule Raman spectroscopy at the junctions of large Ag nanocrystals. *Journal of Physical Chemistry B* 107: 9964–9972.

118. Michaels AM, Jiang J, and Brus L (2000) Ag nanocrystal junctions as the site for surface-enhanced Raman scattering of single Rhodamine 6G molecules. *Journal of Physical Chemistry B* 104: 11965–11971.

119. Shim S, Stuart CM, and Mathies RA (2008) Resonance Raman cross-sections and vibronic analysis of Rhodamine 6G from broadband stimulated Raman spectroscopy. *ChemPhysChem* 9: 697–699.

120. Vosgrone T and Meixner AJ (2005) Surface- and resonance-enhanced micro-Raman spectroscopy of xanthene dyes: From the ensemble to single molecules. *ChemPhysChem* 6: 154–163.

121. Le Ru EC, Blackie E, Meyer M, and Etchegoin PG (2007) Surface enhanced Raman scattering enhancement factors: A comprehensive study. *Journal of Physical Chemistry C* 111: 13794–13803.

122. Lyandres O, Shah NC, Yonzon CR, *et al.* (2005) Real-time glucose sensing by surface-enhanced Raman spectroscopy in bovine plasma facilitated by a mixed decanethiol/mercaptohexanol partition layer. *Analytical Chemistry* 77: 6134–6139.

123. Lyandres O, Yuen JM, Shah NC, *et al.* (2008) Progress toward an *in vivo* surface-enhanced Raman spectroscopy glucose sensor. *Diabetes Technology and Therapeutics* 10: 257–265.

124. Shah NC, Lyandres O, Walsh JT, Glucksberg MR, and Van Duyne RP (2007) Lactate and sequential lactate-glucose sensing using surface-enhanced Raman spectroscopy. *Analytical Chemistry* 79: 6927–6932.

125. Chen K, Leona M, and Vo-Dinh T (2007) Surface-enhanced Raman scattering for identification of organic pigments and dyes in works of art and cultural heritage material. *Sensor Review* 27: 109–120.

126. Whitney AV, Casadio F, and Van Duyne RP (2007) Identification and characterization of artists' red dyes and their mixtures by surface-enhanced Raman spectroscopy. *Applied Spectroscopy* 61: 994–1000.

127. Chen K, Vo-Dinh KC, Yan F, Wabuyele MB, and Vo-Dinh T (2006) Direct identification of alizarin and lac dye on painting fragments using surface-enhanced Raman scattering. *Analytica Chimica Acta* 569: 234–237.

128. Jurasekova Z, Domingo C, Garcia-Ramos JV, and Sanchez-Cortes S (2008) *In situ* detection of flavonoids in weld-dyed wool and silk textiles by surface-enhanced Raman scattering. *Journal of Raman Spectroscopy* 39: 1309–1312.

129. Brosseau CL, Gambardella A, Casadio F, *et al.* (2009) Ad-hoc surface-enhanced Raman spectroscopy methodologies for the detection of artist dyestuffs: Thin layer chromatography-surface enhanced Raman spectroscopy and *in situ* on the fiber analysis. *Analytical Chemistry* 81: 3056–3062.

130. Wustholz KL, Brosseau CL, Casadio F, and Van Duyne RP (2009) Surface-enhanced Raman spectroscopy of dyes: from single molecules to the artists' canvas. *Physical Chemistry - Chemical Physics* 11: 7350–7359.

131. Zhang XY, Young MA, Lyandres O, and Van Duyne RP (2005) Rapid detection of an anthrax biomarker by surface-enhanced Raman spectroscopy. *Journal of the American Chemical Society* 127: 4484–4489.

132. Zhang XY, Zhao J, Whitney AV, Elam JW, and Van Duyne RP (2006) Ultrastable substrates for surface-enhanced Raman spectroscopy: Al2O3 overlayers fabricated by atomic layer deposition yield improved anthrax biomarker detection. *Journal of the American Chemical Society* 128: 10304–10309.

133. Stuart DA, Biggs KB, and Van Duyne RP (2006) Surface-enhanced Raman spectroscopy of half-mustard agent. *Analyst* 131: 568–572.

134. Biggs KB, Camden JP, Anker JN, and Van Duyne RP (2009) Surface-enhanced Raman spectroscopy of benzenethiol adsorbed from the gas phase onto silver film over nanosphere surfaces: Determination of the sticking probability and detection limit time. *Journal of Physical Chemistry A* 113: 4581–4586.

135. Kim JH, Ehrman SH, and Germer TA (2004) Influence of particle oxide coating on light scattering by submicron metal particles on silicon wafers. *Applied Physics Letters* 84: 1278–1280.

136. Chan GH, Zhao J, Hicks EM, Schatz GC, and Van Duyne RP (2007) Plasmonic properties of copper nanoparticles fabricated by nanosphere lithography. *Nano Letters* 7: 1947–1952.

137. Ekinci Y, Solak HH, and Loffler JF (2008) Plasmon resonances of aluminum nanoparticles and nanorods. *Journal of Applied Physics* 104: 083107/083101–083107/083106.

138. Langhammer C, Schwind M, Kasemo B, and Zoric I (2008) Localized surface plasmon resonances in aluminum nanodisks. *Nano Letters* 8: 1461–1471.

139. Lu XM, Au L, McLellan J, *et al.* (2007) Fabrication of cubic nanocages and nanoframes by dealloying Au/Ag alloy

nanoboxes with an aqueous etchant based on $Fe(NO_3)(3)$ or NH_4OH. *Nano Letters* 7: 1764–1769.

140. Doering WE, Piotti ME, Natan MJ, and Freeman RG (2007) SERS as a foundation for nanoscale, optically detected biological labels. *Advanced Materials* 19: 3100–3108.

141. McMahon JA, Wang YM, Sherry LJ, *et al.* (2009) Correlating the structure, optical spectra, and electrodynamics of single silver nanocubes. *Journal of Physical Chemistry C* 113: 2731–2735.

142. Sherry LJ, Chang SH, Schatz GC, *et al.* (2005) Localized surface plasmon resonance spectroscopy of single silver nanocubes. *Nano Letters* 5: 2034–2038.

143. McLellan JM, Li ZY, Siekkinen AR, and Xia YN (2007) The SERS activity of a supported Ag nanocube strongly depends on its orientation relative to laser polarization. *Nano Letters* 7: 1013–1017.

144. McLellan JM, Siekkinen A, Chen JY, and Xia YN (2006) Comparison of the surface-enhanced Raman scattering on sharp and truncated silver nanocubes. *Chemical Physics Letters* 427: 122–126.

145. Camden JP, Dieringer JA, Zhao J, and Van Duyne RP (2008) Controlled plasmonic nanostructures for surface-enhanced spectroscopy and sensing. *Accounts of Chemical Research* 41: 1653–1661.

146. McMahon J, Henry A-I, Wustholz KL, *et al.* (2009) Gold nanoparticle dimer plasmonics: Finite element method calculations of the EM enhancement to surface-enhanced Raman spectroscopy. *Analytical and Bioanalytical Chemistry* 394, doi 10.1007/s00216-009-2738-4.

147. Zou SZ and Weaver MJ (1998) Surface-enhanced Raman scattering on uniform transition metal films: Toward a versatile adsorbate vibrational strategy for solid-nonvacuum interfaces? *Analytical Chemistry* 70: 2387–2395.

148. Pettinger B (2006) Tip-enhanced Raman spectroscopy (TERS). In: *Surface-Enhanced Raman Scattering: Physics and Applications*, vol. 103, pp. 217–240. Berlin: Springer.